Modeled Greenland Ice Sheet evolution constrained by ice-core-derived Holocene elevation histories

Mikkel L. Lauritzen[1], Anne Solgaard[3], Nicholas Rathmann[1], Bo M. Vinther[1], Aslak Grindsted[1], Brice Noël[4], Guðfinna Aðalgeirsdóttir[2], and Christine S. Hvidberg[1]

[1]Niels Bohr Institute, University of Copenhagen, Copenhagen, Denmark
[2]Institute of Earth Sciences, University of Iceland, Reykjavík, Iceland
[3]Geological Survey of Denmark and Greenland, Copenhagen, Denmark
[4]Laboratoire de Climatologie et Topoclimatologie, SPHERES, University of Liège, Liège, Belgium

Correspondence: Mikkel L. Lauritzen (mikkel.lauritzen@nbi.ku.dk)

Abstract. During the Holocene, the Greenland Ice Sheet (GrIS) experienced substantial thinning, with some regions losing up to 600 meters of ice. Ice sheet reconstructions, paleoclimatic records, and geological evidence indicate that during the Last Glacial Maximum, the GrIS extended far beyond its current boundaries and was connected with the Innuitian Ice Sheet (IIS) in the northwest. We investigate these long-term geometry changes and explore several possible factors driving those changes by using the Parallel Ice Sheet Model (PISM) to simulate the GrIS thinning throughout the Holocene period, from 11.7 ka ago to the present. We perform an ensemble study of 841 model simulations in which key model parameters are systematically varied to determine the parameter values that, with quantified uncertainties, best reproduce the 11.7 ka of surface elevation records derived from ice cores, providing confidence in the modeled GrIS historical evolution. We find that since the Holocene onset, 11.7 ka ago, the GrIS mass loss has contributed 5.3±0.3 m to the mean global sea level rise, which is consistent with the ice-core-derived thinning curves spanning the time when the GrIS and the Innuitian Ice Sheet were bridged. Our results suggest that the ice bridge collapsed 4.9±0.5 ka ago and that the GrIS is still responding to these past changes, having raised sea level by 23±26 mm SLE ka^{-1} in the last 500 years. Our results have implications for future ice sheet evolution, which should account for this long-term, transient trend.

1 Introduction

During the Last Glacial Maximum (LGM), approximately 20 ka ago, Earth was covered by large ice sheets, including the Laurentide, Fenno-Scandian, Innuitian, and Greenlandic ice sheets, and the global mean sea level was 125–134 m lower than today (Gulev et al., 2021). Geological evidence suggests that the Greenland Ice Sheet (GrIS) extended to the continental shelf and was connected to the Innuitian Ice Sheet (IIS) at the Nares Strait (England et al., 2006).

Towards the end of the last glacial period, the Bølling-Allerød interstadial brought an abrupt warming to the Northern Hemisphere 14.7 ka ago, followed by the cooling of the Younger Dryas stadial 12.9 ka ago (Rasmussen et al., 2006). The Holocene interglacial began 11.7 ka ago, bringing temperatures that were locally up to 15°C warmer in Greenland (Andersen et al., 2004). However, temperature reconstructions vary by several degrees, which can significantly affect the modeled GrIS

history (Nielsen et al., 2018). Following the Holocene Thermal Maximum, 6-9 ka ago, Greenland temperatures have shown a long-term decreasing trend (Vinther et al., 2009), but anthropogenic forcing has since reversed the course of natural temperature change, resulting in a global increase in temperatures since pre-industrial times (Eyring et al., 2021).

Accurately modeling the historical evolution of the GrIS is essential for evaluating and calibrating ice sheet models. Ice sheet models respond to climate change over a range of timescales and are rarely in steady state (e.g. Lauritzen et al., 2023). However, several ice sheet model studies have overlooked a calibration of their temporal evolution and only focused on the evolution of ice temperature, neglecting other delayed responses, such as bedrock dynamics. For example, the ISMIP6 protocol does not require calibration (Nowicki et al., 2020), and most of the ISMIP6 ensemble simulations underestimate the observed IMBIE consensus mass loss from the GrIS (The IMBIE Team, 2020; Aschwanden et al., 2021). Recent advances have addressed this by calibrating an ice sheet model to satellite-based gravimetry-derived mass loss data of the GrIS (Aschwanden and Brinkerhoff, 2022), but the satellite-based calibration data period only covers 22 years at the time of writing, and there is no guarantee that it gives a sensible long term response.

Calibrating the model to align with present-day observations of ice thickness and velocities risks capturing only the present-day state while being on a wrong state trajectory; that is, neglecting the long-term memory of the ice sheet and the response of the bedrock to past changes in ice load. These differences in past trajectories affect the projected future mass loss in this century as demonstrated by Aðalgeirsdóttir et al. (2014).

Before the satellite era ice sheet modeling must rely on proxy data from paleo-climatic records and ice extent markers for constraining and validating the long-term transient response of the ice sheet (state trajectory) over these considerably longer timescales. Surface elevation histories, derived from deep ice cores at Camp Century (CC), NGRIP, GRIP, and Dye 3 (See Fig. 1), provide such constraints for modeling the GrIS through the Holocene (Vinther et al., 2009). These archives offer valuable insights into the ice sheet's dynamics through the past climate and significantly enhance the robustness of model predictions.

Previous studies have attempted to model elevation changes derived from ice cores. Notably, Lecavalier et al. (2017) modeled Holocene surface elevation changes at CC using temperature anomalies from the Agassiz ice cores, suggesting that early Holocene temperatures were 7 K higher than today. However, they did not account for the buttressing effect of the IIS, a key driver of thinning (MacGregor et al., 2016), and focused only on relative elevation changes, without reconstructing absolute elevation history. More recently, Tabone et al. (2024) modeled elevation changes at the GRIP site, attributing them to the onset of the Northeast Greenland Ice Stream (NEGIS).

In this study, we use the Parallel Ice Sheet Model (PISM) to model the long-term transient response of the GrIS to past climatic changes and the collapse of the IIS bridge during the Holocene. By varying 20 key model parameters in an ensemble of 841 members, we show that it is possible to model the ice-core-derived elevation histories rather than just the thinning *if* the grounding line can advance to the continental shelf *and* the GrIS can connect to the IIS. We use this setup to constrain the model parameters for the ensemble and to estimate the GrIS long-term evolution with quantified uncertainties. Using the calibrated model, we investigate the Holocene ice sheet mass loss and assess the ongoing long-term response of the modeled GrIS and bedrock dynamics.

2 Paleoclimatic evidence

When water evaporates over the oceans and precipitates over the GrIS, a fractionation process changes the ratio between the oxygen isotopes in the water. This process is temperature dependent, a relationship first used by Dansgaard et al. (1969) to infer past temperatures from measurements of oxygen isotopes at CC. The temperatures over the GrIS change locally due to both regional temperature changes and due to surface elevation changes. Vinther et al. (2009) derived a GrIS-wide temperature signal by assuming that the Renland and Aggasiz ice core sites are located within restricted ice domes where ice thickness remains constant. This GrIS-wide temperature signal was then subtracted from the oxygen isotope signals at CC, NGRIP, GRIP, and Dye 3 to derive local surface elevation histories, after correcting for upstream effects.

We use five different ice-core-based temperature anomaly reconstructions described by Nielsen et al. (2018) to account for uncertainty in the past temperatures. The temperature reconstructions are shown in Fig. A1. Reconstructions 1 and 2 use the GRIP ice core with linear and quadratic transfer functions from Huybrechts (2002) and Johnsen et al. (1995), respectively. Reconstruction 3 uses the NGRIP core with the same transfer function from Huybrechts (2002), while reconstruction 4 is the GrIS-wide reconstruction from Vinther et al. (2009), the only one accounting for elevation change. Reconstruction 5 is based on the NGRIP core with an isotope diffusion inversion scheme (Gkinis et al., 2014). Reconstruction 1 was used by the SeaRISE project (Bindschadler et al., 2013). The Holocene climate in Greenland began with an abrupt warming of approximately 15°C at the glacial-interglacial transition 11.7 ka ago, followed by the Holocene Thermal Maximum around 8-5 ka ago with temperatures 2-3°C higher than the 20th century mean, and then a general cooling trend until the late 20th century. The Holocene Thermal Maximum is only captured by reconstructions 3, 4, and 5, while reconstructions 1 and 2 suggest a more constant Holocene climate.

3 Model setup

To model the Holocene evolution of the GrIS, we use the open-source Parallel Ice Sheet Model (PISM) version 2.1 (Bueler and Brown, 2009; Winkelmann et al., 2011) at 20 km resolution for the spin-up, refined to 10 km for the last 20 ka. PISM is a three-dimensional thermomechanically-coupled model that solves both the Shallow Ice Approximation (SIA) and Shallow Shelf Approximation (SSA) in a hybrid scheme, capturing both slow-moving interior flow and fast flow in ice streams and outlet glaciers. At the ice-ocean boundary, PISM includes sub-grid parameterizations to model grounding line advance and retreat (Gladstone et al., 2010). Model parameters, listed in Table 1, will be varied in our ensemble simulations unless otherwise specified.

3.1 Model domain

The model domain, shown in Fig. 1, spans 6.7 $\times 10^6$ km^2, from the continental shelf in the east to the Canadian Arctic Archipelago in the west. A north polar stereographic projection with a standard parallel at 70° N and central longitude of -45° W (ESPG 3413) is used. The projection introduces distortions of up to +5% in the north and -11% in the southwest relative

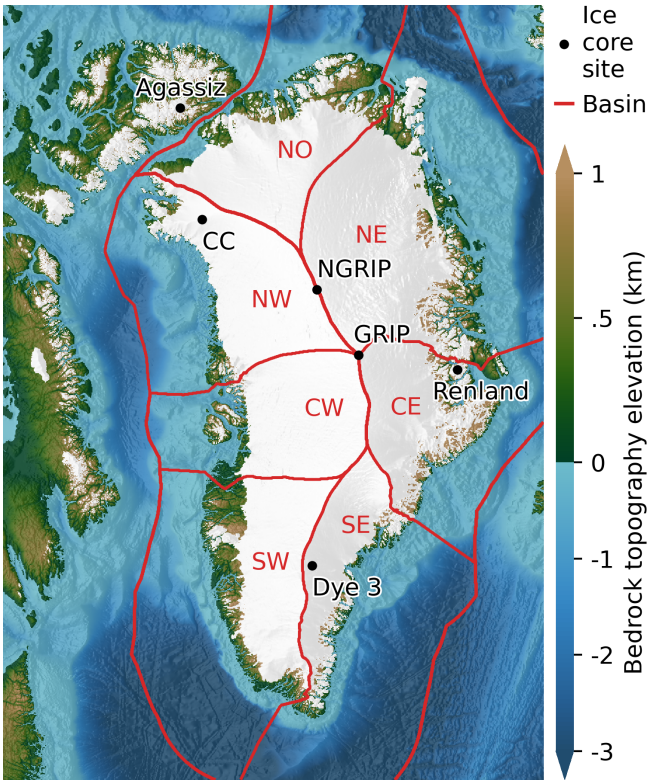

Figure 1. Model domain showing the present-day bedrock topography elevation from Morlighem (2022), Jakobsson et al. (2020), and GEBCO Bathymetric Compilation Group (2023) and the present-day ice cover from Morlighem (2022) and RGI Consortium (2023) shown in white. The ice core sites discussed in the text (CC, NGRIP, GRIP, Dye 3, Renland, and Agassiz) are shown on top together with the glacier catchment basins (NW, CW, SW, SE, CE, NE, NO) from Mouginot and Rignot (2019) and extended out to the Exclusive Economic Zone of Greenland (Flanders Marine Institute (VLIZ), Belgium, 2023) and constitute our extended continental shelf (ECS) domain, see text.

to the central latitude and longitude. PISM uses a flat earth approximation, so volume is not conserved when transforming thickness between projections. Volumes and mass loss rates are reported using the actual grid area.

To partition mass between Greenland and Canada, we introduce an Extended Continental Shelf (ECS) mask, corresponding to Greenland's Exclusive Economic Zone (Flanders Marine Institute (VLIZ), Belgium, 2023). This divides the two regions at the Nares Strait and Baffin Bay, extending to the continental shelf in the north, east, and south. For mass loss partitioning when the grounding line advances, we extend the basins from Mouginot and Rignot (2019) to the ECS using nearest neighbor extrapolation.

The present-day bedrock topography over Greenland is from BedMachine v5 (Morlighem, 2022), and extended with IBCAO v4.2 (Jakobsson et al., 2020) and GEBCO Bathymetric Compilation Group (2023) to cover the larger domain, in that order of preference to get the best bedrock available.

At the lateral boundary, a Dirichlet boundary condition of zero ice thickness is used, and the influence of the majority of the Laurentide Ice Sheet is thereby neglected. The north and south are bounded by the open ocean, while Iceland and Svalbard are just visible towards the east. At the base of a 2 km deep bedrock thermal layer, the thermal heat flux from Shapiro (2004) is applied constantly in time.

3.2 Surface mass balance

Determining the surface mass balance (SMB) of the GrIS is challenging, and regional climate models (RCMs), such as RACMO, not only simulate the atmospheric conditions over the GrIS but also incorporate a detailed snowpack model to simulate precipitation, melt, percolation, refreezing, and sublimation processes (Noël et al., 2019).

Given the complexity of including all these processes, it is not feasible to run the RCM over thousands of years, as needed in our study, and we instead apply a Positive Degree Day (PDD) scheme to calculate the surface melting. This approach bases the SMB solely on temperature, T, and precipitation, P. In the PDD scheme, surface melt is proportional to the extent to which the temperature exceeds the freezing point (e.g. Braithwaite, 1985). We use two constants of proportionality: one for snow, f_s, and another for ice, f_i.

To force the PDD model, we use a 12-month reference climatology based on the multi-year monthly averages of temperature and precipitation for the period 1960–1989 from the RACMO RCM. Since our model domain is not covered by a single RACMO simulation, we combine different simulations (see Fig. A3). We looked at three areas for rainfall data: Greenland, the Northern Canadian Arctic Archipelago, and the Southern Canadian Arctic Archipelago (Noël et al., 2018), treating areas outside these regions as having no rainfall. For temperature, we used RACMO2.3p2 at 5.5 km for Greenland (Noël et al., 2019) and combined it with a broader 11 km simulation (Noël et al., 2015) for the rest of the area. The mean precipitation and summer temperatures from the resulting climatology are shown in Fig. A2.

We account for historical temperature changes using the same domain-wide anomalies as in Nielsen et al. (2018), i.e., by adding a domain-wide, spatially uniform temperature anomaly, ΔT, that varies in time, and a lapse rate adjustment, Γ, of the surface temperature relative to the RCM surface topography. Since the vapor pressure approximately scales exponentially with temperature in the Clausius-Clapeyron relation, we account for historical precipitation changes by scaling the reference precipitation field with a time-dependent scaling factor $\exp(\omega(\phi)\Delta T(t))$. Here, ω has the latitude dependence

$$\omega(\phi(x,y)) = \begin{cases} \omega_\downarrow & \phi \le \phi_\downarrow \\ \omega_\downarrow + \dfrac{\phi - \phi_\downarrow}{\phi_\uparrow - \phi_\downarrow}(\omega_\uparrow - \omega_\downarrow) & \phi_\downarrow \le \phi \le \phi_\uparrow \\ \omega_\uparrow & \phi_\uparrow \le \phi \end{cases}, \tag{1}$$

where ϕ is the latitude and $\phi_\downarrow = 60^\circ N$ and $\phi_\uparrow = 75^\circ N$ are chosen to cover most of Greenland. In this way, we allow for different precipitation histories in Northern and Southern Greenland, unlike the uniform scaling used by many previous modeling attempts (e.g. Nielsen et al., 2018).

3.3 Ocean forcing

Following Aschwanden et al. (2019) we take the sub-shelf ocean melt to be separable in space and time

$$\dot{m}(x,y,t) = \dot{m}_x(\phi(x,y))\dot{m}_t(t), \tag{2}$$

with the spatial dependence controlling the present-day melt rate given by

$$\dot{m}_x(\phi(x,y)) = \begin{cases} \dot{m}_\downarrow & \phi \le \phi_\downarrow \\ \dot{m}_\downarrow + \dfrac{\phi - \phi_\downarrow}{\phi_\uparrow - \phi_\downarrow}(\dot{m}_\uparrow - \dot{m}_\downarrow) & \phi_\downarrow \le \phi \le \phi_\uparrow \\ \dot{m}_\uparrow & \phi_\uparrow \le \phi \end{cases}, \tag{3}$$

where $\phi_\downarrow = 71^\circ N$ and $\phi_\uparrow = 80^\circ N$, following Aschwanden et al. (2019), while $\dot{m}_\downarrow$ and $\dot{m}_\uparrow$ are the upper and lower melt values which we will vary. To allow the formation of an ice bridge to Canada, the sub-shelf melt rate is scaled by

$$\dot{m}_t(t) = \begin{cases} 0 & t \le \tau \\ \dfrac{t-\tau}{\Delta\tau} & \tau \le t \le \tau + \Delta\tau \\ 1 & \tau + \Delta\tau \le t \end{cases}, \tag{4}$$

such that there will be no ocean melt for times earlier than τ, while it increases to present-day values in the time $\Delta\tau$ inspired by the rapid change in ocean temperatures found by Clark et al. (2020). In addition to sub-surface melt, ice is calved off at the oceanfront at a rate that is proportional to the tensile von Mises stress and inversely proportional to a characteristic parameter, σ_{max} (Morlighem et al., 2016). Additionally, all ice thinner than H_{cr} is calved off, and a eustatic sea level forcing from Imbrie and McIntyre (2006) is applied, changing the ocean level by 130 m in the last 19 ka.

3.4 Ice dynamics

The constitutive relation that relates the strain rate, $\dot{\epsilon}_{ij}$, to the stress, τ_{ij}, in the ice sheet is

$$\dot{\epsilon}_{ij} = EA\tau_{\text{e}}^{n-1}\tau_{ij}, \tag{5}$$

where E is the enhancement factor, τ_{e} is the effective deviatoric stress, n is the creep exponent, and A is the ice softness which depends on temperature, pressure, and water content of the ice. The enhancement factor and the creep exponents are taken to be different for the SIA and the SSA. We use $E_{\text{SSA}} = 1.3, n_{\text{SIA}} = 3$ while varying E_{SIA} and n_{SSA} following Aschwanden and Brinkerhoff (2022). The basal sliding velocity $\mathbf{u}_{\text{b}}$ in the SSA is related to the basal shear stress τ_{b} through the pseudo-plastic power law:

$$\tau_{\text{b}} = -\tan(\phi) N_{\text{till}} \frac{\mathbf{u}_{\text{b}}}{u_{\text{th}}^q |\mathbf{u}_{\text{b}}|^{1-q}}, \tag{6}$$

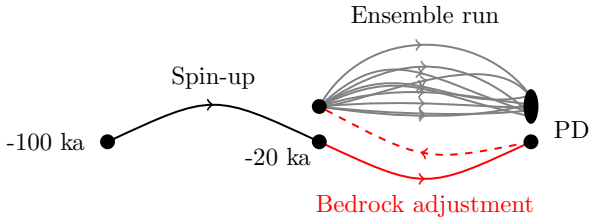

Figure 2. Schematic of the model ensemble experiment. The ice sheet is initialized at -100 ka using present-day geometry and run through the last glacial at 20 km resolution. The bedrock is then iteratively updated at -20 ka to reduce the modeled present-day bedrock topography deviation. After finding a suitable bedrock topography, the ice sheet model is branched off at -20 ka, and an ensemble of simulations is run at 10 km resolution. While the x-axis depicts time, the y-axis is only used to reflect that the states differ.

where q is the sliding exponent, $u_{\text{th}} = 100$ m a^{-1} is a characteristic speed. The till friction angle, ϕ, is parameterized as a continuous function of bedrock topography that increases linearly from ϕ_{min} to ϕ_{max} between z_{min} and z_{max}. The effective pressure on the till N_{till} depends on the water level in the till, W_{till}, and the overburden pressure of the ice, P_0:

$$N_{\text{till}} = \min\left\{P_0, \tilde{N}_0 \left(\frac{\delta P_0}{\tilde{N}_0}\right)^{W_{\text{till}}/W_{\text{till}}^{\text{max}}}\right\}, \tag{7}$$

where $W_{\text{till}}^{\text{max}} = 2$ m is the maximal water level in the till and $\tilde{N}_0 = 5.6 \times 10^8$ Pa is a reference pressure simplified from the original formulation of Bueler and van Pelt (2015) to include the dependence of the till compressibility and the till void ratio. δ controls the lower bound of the effective pressure, which we will vary in our simulations.

3.5 Earth deformation and initialization

The bedrock responds to changes in ice load by the visco-elastic bed deformation model by Lingle and Clark (1985) and Bueler et al. (2007) with flexural rigidity $D = 5 \times 10^{24}$ N m and upper mantle viscosity $\eta = 1 \times 10^{21}$ Pa s.

We initialize the GrIS by running the model from -100 ka to -20 ka (all times are relative to 2 ka CE) at 20 km grid resolution using the parameters listed in Table 1 and with initial bedrock topography taken to be the same as the present day (Morlighem, 2022; Jakobsson et al., 2020; GEBCO Bathymetric Compilation Group, 2023).

Since we only know the bedrock elevation for the present day and not for the past, we iteratively adjust the bedrock at -20 ka (as shown in Fig. 2) to ensure that the modeled bedrock topography at the end of the simulations closely matches the observed present-day topography. A simulation with 20 km resolution is run from -20 ka to the present, and the deviation of the modeled bedrock from the observed topography is used to update the bedrock at -20 ka according to

$$b^0_{i+1} = b^0_i + K(b^{\text{obs}} - b^1_i), \tag{8}$$

where b^{obs} is the observed present-day topography (Morlighem, 2022; Jakobsson et al., 2020; GEBCO Bathymetric Compilation Group, 2023), b^0_i is the modeled bedrock topography at -20 ka, and b^1_i is the modeled bedrock topography at the present

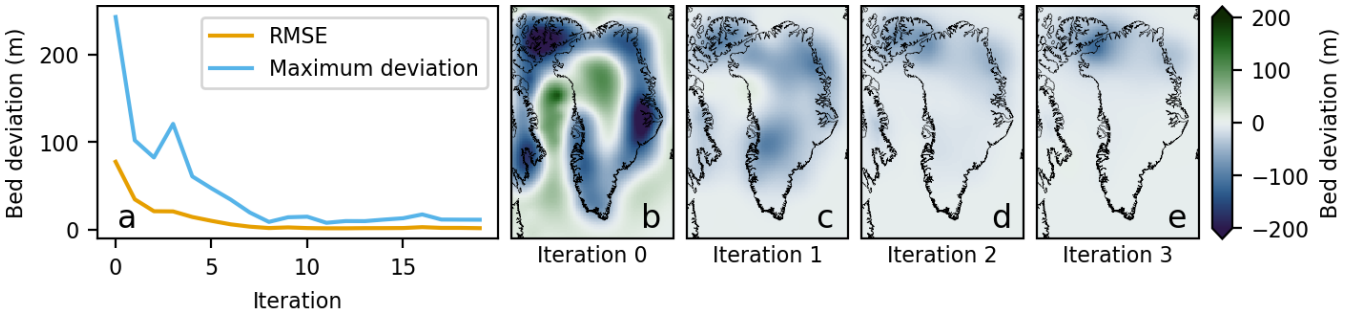

Figure 3. Iterative bedrock adjustment. (a) The modeled present-day bedrock elevation deviation compared to (Morlighem, 2022; Jakobsson et al., 2020; GEBCO Bathymetric Compilation Group, 2023). (b–e) shows the zeroth to the third iteration of the modeled present-day bedrock elevation deviation from observed.

day. The relaxation parameter $K = 0.7$ is used to prevent overcompensation from any potential positive feedback associated with the updated bedrock, although such feedback may not be significant, given that the bedrock–mass balance feedback is likely negative. After 20 iterations, the RMSE of the bedrock decreased from 77.4 m to 3.3 m, as shown in Fig. 3. The impact of these iterations on the surface elevation is illustrated in Fig. A7.

At -20 ka, the simulation is branched using the adjusted bedrock (b^0) from the previous step (shown in Fig. A9), and an ensemble of simulations is run at a 10 km grid resolution until the present day, varying the 20 key parameters listed in Table 1.

4 Bayesian inference

To account for model uncertainty and assess the importance of model parameters, we run an ensemble of simulations from -20 ka to the present, varying the 20 parameters listed in Table 1. The dynamic parameters are based on those varied by Aschwanden and Brinkerhoff (2022), while the oceanic and atmospheric parameters are introduced in sections 3.2 and 3.3.

To effectively sample the parameter space, 841 parameters are drawn using the second-order orthogonal Latin Hypercube Sampling (LHS) design (Tang, 1993). This ensures that all pairs of parameters are sampled uniformly and reduces the risk of clustering.

For each of the four ice core sites, we calculate the likelihood of observing the ice-core-derived elevation history given the modeled elevation change with model parameters $\mathbf{m}$:

$$\rho(\mathbf{h}_i^{\text{obs}}|\mathbf{m}) \propto \prod_j \exp\left(-\frac{\left(h_{i,j}(\mathbf{m}) - h_{i,j}^{\text{obs}}\right)^2}{2\sigma_i^2\beta}\right), \tag{9}$$

where i denotes the ice core site, and j is the time step of the ice core samples to which modeled elevations are interpolated. σ_i are the uncertainties from Vinther et al. (2009), derived from the spread of $\delta^{18}O$ values in two parallel records from the Agassiz Ice Cap and the uncertainty in bedrock uplift at the Agassiz and Renland sites. The lapse rate uncertainty used to derive elevation changes is not included. Present-day and past elevations are weighted equally to avoid biasing the likelihoods toward

Parameter	Description	Spin-up	Range	Estimates				
				Combined	CC	NGRIP	GRIP	Dye 3
Atmosphere								
ΔT	Temperature reconstruction	3	1—5	1	1	4	2	3
f_s	PDD param. snow (mm K^{-1} d^{-1})	5.04	5.7—8.9	6.5±0.7	7.1±0.8	7±1	7.5±0.7	7.8±1.0
f_i	PDD param. ice (mm K^{-1} d^{-1})	12.5	7—10	7.7±0.6	8.5±0.8	8.6±0.8	8.7±0.9	8.4±0.7
Γ	Atmospheric lapse rate (K km^{-1})	5	4—9	5.4±0.7	7±1	6±1	6±1	6±1
$\omega_\downarrow$	Southern precip. scaling (% K^{-1})	5	0—4.5	2±1	2±1	2±1	2±1	2±1
$\omega_\uparrow$	Northern precip. scaling (% K^{-1})	7	0—9	2±1	3±2	2±1	4±2	3±2
Ocean								
H_{cr}	Threshold for thickness calving (m)	50	50—150	96±17	87±25	97±30	112±30	106±30
σ_{max}	Characteristic stress (MPa)	1	0.8—1.2	0.92±0.09	1.03±0.10	1.0±0.1	1.0±0.1	1.0±0.1
$\dot{m}_\downarrow$	Melt rate south of 71°N (m a^{-1})		300—500	394±29	409±65	400±56	391±56	391±50
$\dot{m}_\uparrow$	Melt rate north of 80°N (m a^{-1})		10—30	20±6	19±6	21±6	19±6	19±5
τ	Ocean melt onset (ka)		4—8	5.6±0.6	5.5±0.7	6±1	6±1	6±1
$\Delta\tau$	Ocean melt set in time (ka)		0—2	1.1±0.5	1.1±0.6	0.9±0.6	1.0±0.6	0.7±0.6
Dynamics								
n_{SSA}	Creep exponent for the SSA (1)	3.3	3.2—3.4	3.28±0.04	3.35±0.04	3.33±0.04	3.25±0.04	3.23±0.03
E_{SIA}	Enhancement factor for the SIA (1)	3	2.5—3.3	3.0±0.2	2.7±0.2	2.9±0.2	3.1±0.2	3.1±0.2
q	Basal sliding power coefficient (1)	0.8	0.7—0.9	0.82±0.05	0.79±0.05	0.81±0.06	0.80±0.06	0.83±0.06
δ	Effective pressure parameter (%)	2	1.5—2.5	2.1±0.2	2.0±0.2	2.0±0.3	2.0±0.3	2.1±0.3
ϕ_{min}	Minimal till friction angle (°)	10	5—10	8±1	8±1	7±1	7±1	8±1
ϕ_{max}	Maximal till friction angle (°)	42	40—45	43±1	43±2	42±1	43±1	43±1
z_{min}	Till friction cutoff elevation (m)	-700	-600—-300	-421±60	-481±80	-443±84	-433±80	-447±77
z_{max}	Till friction cutoff elevation (m)	700	0—500	271±172	238±118	231±134	252±154	271±146

Table 1. List of the 20 parameters that are varied in our ensemble of simulations. The temperature reconstruction is sampled discretely. The estimated parameter values are given as the mean plus minus the standard deviation of the posterior PDFs except for the temperature reconstruction, which is the mode of the posterior PDFs.

the present configuration. Following Aschwanden and Brinkerhoff (2022), we introduce $\beta = 100$ to account for autocorrelation in the uncertainties, reducing the degrees of freedom by a factor of 100, which corresponds to a decorrelation time of 2000 years.

Additionally, we calculate the combined likelihood of the ice-core-derived elevation changes for all sites, which is proportional to the product of the individual likelihoods, assuming no spatial correlation between the drill sites:

$$\rho(\mathbf{h}^{\text{obs}}|\mathbf{m}) \propto \prod_{i=1}^{4} \rho(\mathbf{h}_i^{\text{obs}}|\mathbf{m}). \tag{10}$$

The parameters are sampled uniformly over the ranges specified in Table 1, which focuses on the volume of parameter space that shows the highest likelihood in an initial ensemble of simulations.

The posterior joint probability density functions (PDFs) are then given by Bayes's theorem:

$$\rho(\mathbf{m}|\mathbf{h}_i^{\text{obs}}) = \frac{\rho(\mathbf{h}_i^{\text{obs}}|\mathbf{m})}{\rho(\mathbf{h}_i^{\text{obs}})}\rho(\mathbf{m}), \tag{11}$$

where the prior distribution $\rho(\mathbf{m})$ is taken to be uniform within the intervals listed in Table 1. From the five posteriors, we get five PDFs of ice sheet evolution through the Holocene from which we estimate relevant observables listed in Table 2. Unless stated otherwise, all model results are based on the combined posterior PDF.

To evaluate the effectiveness of the sampling, we compute the effective sampling size for each of our five posteriors:

$$n_{\text{eff}} = \frac{\sum_k \rho(\mathbf{h}_i^{\text{obs}}|\mathbf{m}_k)^2}{\left(\sum_k \rho(\mathbf{h}_i^{\text{obs}}|\mathbf{m}_k)\right)^2}, \tag{12}$$

where k denotes the sample member.

Although constraining the simulations to present-day observations would increase confidence in our modeled present-day state, we avoid doing so because this study focuses on the transient evolution of the GrIS and how the ice-core-derived surface elevation histories from Vinther et al. (2009) can be used to constrain the ice sheet's evolution.

5 Results

5.1 Surface elevation evolution

Figure 4 shows the modeled and the ice-core-derived surface elevations during the Holocene for the four ice-core sites. The individual estimates (green) for each site match the observed (blue) and reproduce the large thinning observed at CC and Dye 3 as well as the more moderate thinning in the interior at GRIP and NGRIP with RMSEs between 12 and 53.6 m. The combined estimated elevation (orange) is lower at CC and Dye 3 at the Holocene onset, while it is too high at GRIP compared to the individual estimates. The bedrock and ice thickness history associated with the surface elevation changes are shown in Fig. A8.

To illustrate the effect of allowing the ice sheet to advance beyond its present-day boundaries, we ran two additional simulations: one restricted from advancing beyond the present-day GrIS coast and another restricted from advancing beyond the ECS mask. Both simulations started from the unrestricted branch-off point at -20 ka and used the same parameters as the ensemble member with the highest combined likelihood, although these parameters may not necessarily be optimal for either of the restricted runs. The simulation restricted to the present-day GrIS coast could not reproduce the observed surface elevation history at CC, NGRIP, and Dye 3, showing the importance of a dynamic grounding line. The simulation restricted to not advancing beyond the ECS performed better but also failed to reproduce the thinning at CC, showing the effect of including the Canadian Arctic Archipelago when modeling the GrIS Holocene history. The RMSEs to the four ice-core-derived elevation histories are listed in Table 2 for the five estimates.

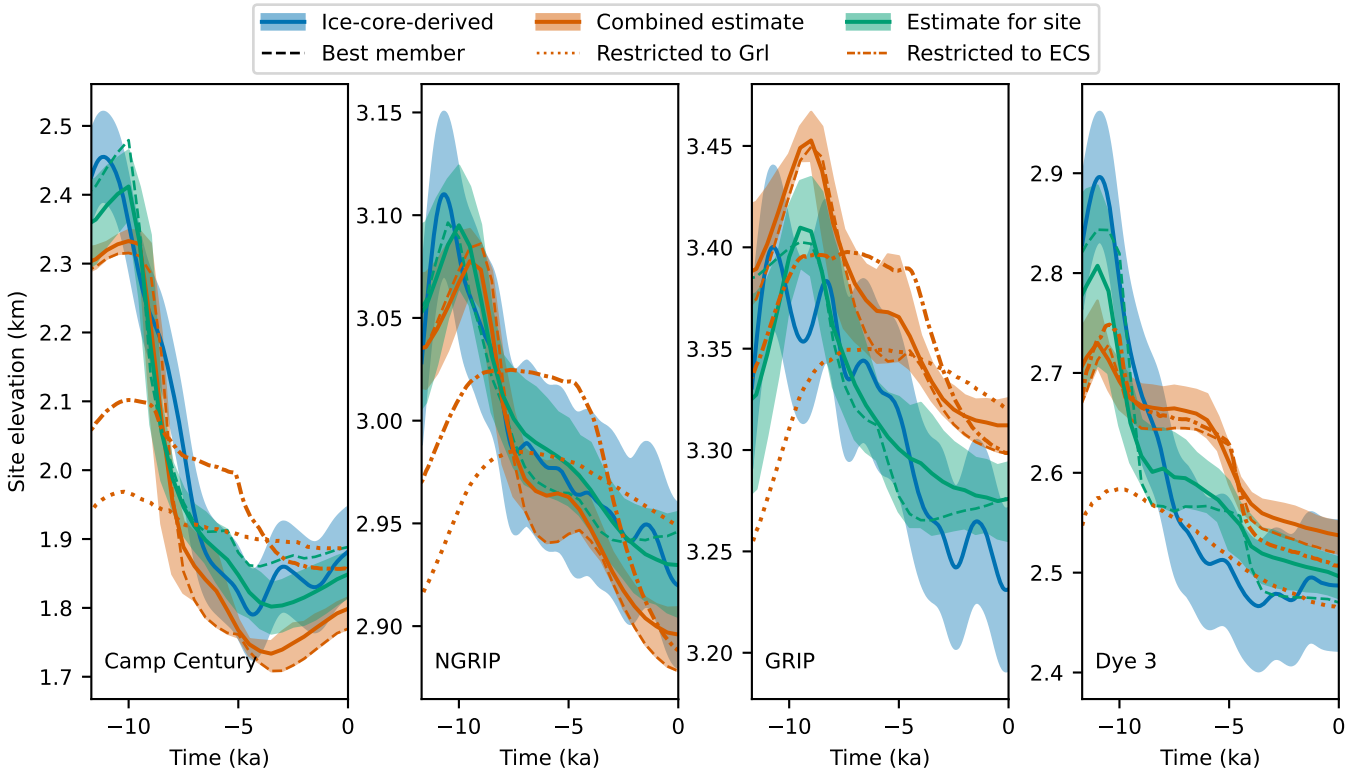

Figure 4. Observed and modeled surface elevation over the last 11.7 ka for the ice core sites, Camp Century (CC), NGRIP, GRIP, and Dye 3. The blue lines are the ice-core-derived surface elevations from Vinther et al. (2009), and the blue envelopes denote one standard deviation. The orange solid lines represent the combined estimate for all sites, while the green solid lines are the individual estimates for each ice core site. The shaded orange and green envelopes denote the estimated 16-84 quantile ranges. The dashed lines are the ensemble members with the highest likelihood for each site (green) and the highest combined likelihood (orange). The orange dotted and dash-dotted lines are simulations with the same parameters as the best ensemble member but restricted to ECS (dash-dotted) and the present-day land margin of the GrIS (dotted).

5.2 Inferred parameters

The ice-core-derived surface elevation histories help constrain the model parameters, and the marginal PDFs for each of the five posteriors are shown in Fig. 5. The estimated parameter values are listed in Table 1, though they vary in how well they are constrained and differ across ice core sites.

Notably, the estimated enhancement factor of the SIA, E_{SIA}, differs substantially between the sites. At CC, it is estimated to be 2.7 ± 0.2, while at GRIP, it is estimated to be 3.1 ± 0.2. The estimated creep exponent for the SSA, n_{SSA} also varies between the sites and has a higher estimate for CC and NGRIP than for GRIP and Dye 3.

Of the five temperature reconstructions, reconstruction 1, which is the coldest throughout the Holocene, has the highest combined likelihood at 61% and the highest likelihood for CC at 40%, where the largest thinning occurs. Reconstruction 2 from

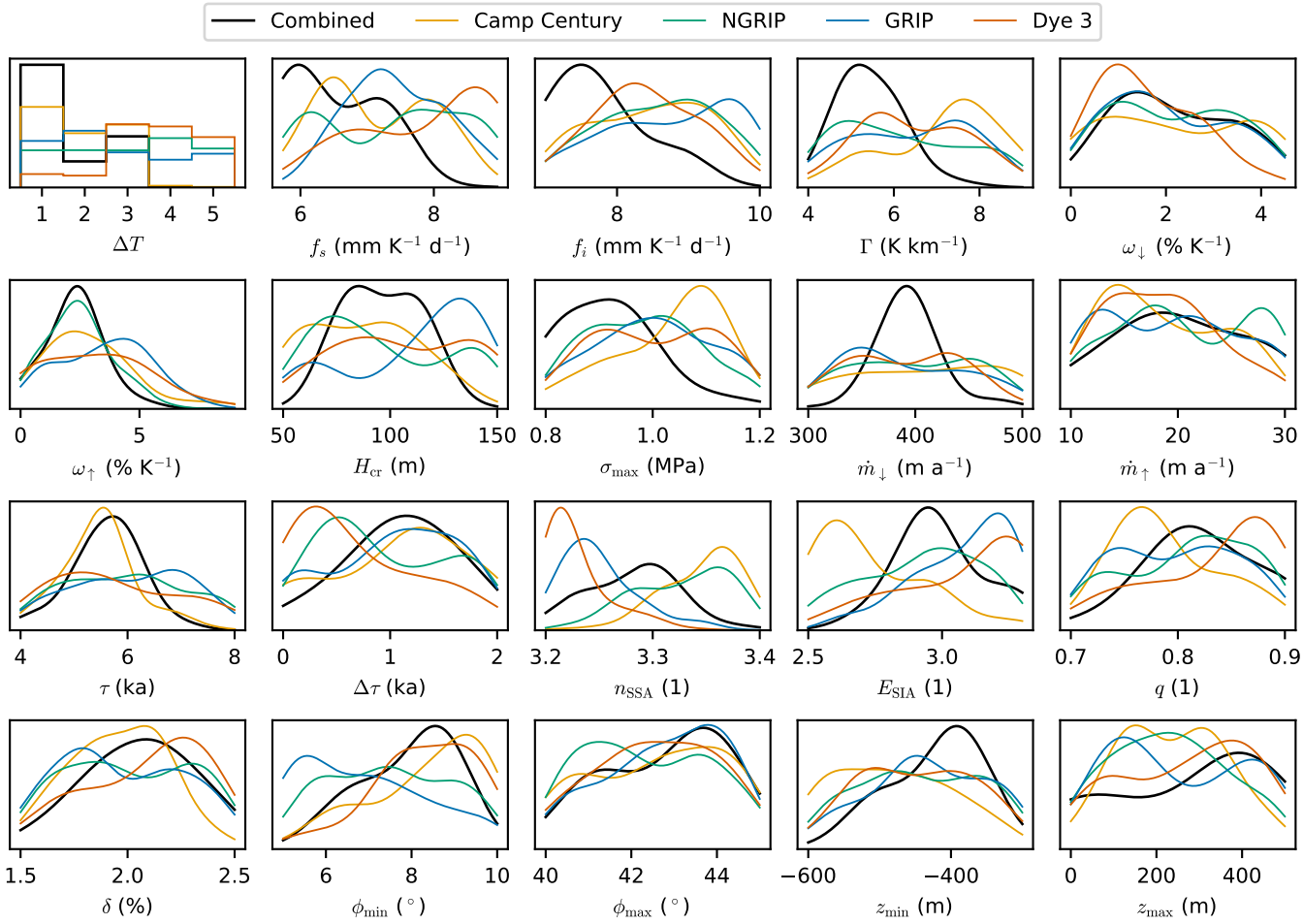

Figure 5. Kernel density estimates of the inferred marginal PDFs for the 20 model parameters that we varied. The units on the y-axes are the inverse of that of the x-axes.

GRIP is more than a degree warmer in the early Holocene and does not perform as well as reconstruction 1. Reconstructions 4 and 5 are the warmest throughout the Holocene and have near-zero likelihood at CC, although reconstruction 4 is the most likely for NGRIP and Dye 3.

The northern precipitation parameter, $\omega_\uparrow$, is more constrained by the northern sites CC and NGRIP, where it has the most influence. Likewise, the southern precipitation parameter, $\omega_\downarrow$, is most constrained by Dye 3. Both parameters are estimated to be $2\pm1\%$ K^{-1} which is substantially lower than the default of 7.3% K^{-1} introduced by Huybrechts (2002) resulting in less accumulation in the warm periods of the Holocene and more accumulation in the cold glacial where the ice sheet builds up.

The onset of sub-shelf ocean melt is well constrained by CC, occurring at 5.6 ± 0.6 ka before present.

5.3 Modeled Holocene evolution

From the branch-off point at -20 ka until the onset of the Holocene (11.7 ka ago), the modeled ice sheet bridges the gap between Canada and Greenland across the Baffin Bay and the Nares Strait. Figure 6 shows the ice sheet configuration at -12 ka, -9 ka, and the present day, while Fig. 7 presents the volume and area evolution from the branch-off point to the present. The model clearly responds to the change in resolution at the branch-off point, showing a positive drift in volume, though this shock appears to have stabilized before the start of the Holocene. By -12 ka, the ice sheet reaches its glacial maximum extent, grounding on the continental shelf and through the Nares Strait.

At -12 ka, the GrIS has a modeled grounded area of 2.96 ± 0.03 km^2, within the ECS. This is 49% or $0.98 \pm 0.05 \times 10^6$ km^2 larger than the present-day modeled area and it is 0.9% larger than the minimum LGM extent and 5.6% smaller than the maximum LGM extent from Leger et al. (2024). Compared to the modeled present-day GrIS, the modeled grounded volume is 6.6 ± 0.4 m SLE larger at -12 ka. Additionally, the grounded volume above flotation is 5.3 ± 0.3 m SLE larger, which contributed to the global mean sea level rise.

Outside the ECS the IIS and Laurentide Ice Sheet are cut off at the domain boundary with a Dirichlet boundary condition of zero thickness. This moves the ice divide at Baffin Island further to the east than if it had been connected to a complete Laurentide Ice Sheet. Together they have a grounded area of $1.20 \pm 0.03 \times 10^6$ km^2 and a grounded volume of 5.0 ± 0.2 m SLE.

During the Holocene collapse of the IIS, the ice divide at the GrIS moves towards the west and the ice streams reorganize in northern Greenland as shown in Fig. 6. This divide migration could explain the onset of NEGIS, as found by Franke et al. (2022), and the shutdown of the older, more northern ice stream, as observed by Jansen et al. (2024).

Figure 8 shows the rate of change of grounded ice for the ensemble member with the highest combined likelihood for the seven basins of the GrIS. The GrIS rate of change becomes negative at -10.7 ka and exhibits two distinct peaks: one at -7.8 ka, with a mass loss rate of 548 Gt a^{-1}, and another at -4.95 ka, following the onset of sub-shelf melting, with a mass loss rate of 511 Gt a^{-1}. It continues to be negative for the rest of the Holocene except for a few times during the last 2 ka, where the average mass loss rate is 23.7 Gt a^{-1}. The mass loss rates are averaged over 50 years.

5.4 Present-day configuration

The modeled present-day extent of grounded ice deviates from the observed extent, as shown in Fig. 9a. Most notably, the modeled extent is larger in the Canadian Archipelago, while it fails to cover an area of 0.08 ± 0.01 km^2 and inaccurately covers an area of 0.19 ± 0.01 km^2 compared to the observed GrIS extent. This comparison includes peripheral glaciers and excludes ice thinner than 10 meters, which is considered to be seasonal.

The modeled GrIS grounded volume at present day is 9.1 ± 0.1 m SLE, which is 1.5 m SLE larger than the observed grounded volume, including peripheral glaciers (Morlighem, 2022). This discrepancy can be attributed to the ice thickness deviations at the GrIS margin, as shown in Fig. 9b.

Observable	Estimates						Restricted	
	Combined	CC	NGRIP	GRIP	Dye 3	Prior	Grl	ECS
Elevation history RMSE								
CC (m)	88.1	53.6	116.8	154.3	170.7	119	223.4	165.9
NGRIP (m)	26.8	44.9	12	69.8	69.4	34.9	67.8	49.9
GRIP (m)	58.6	123	86	27.2	29.5	62	64.5	59.5
Dye 3 (m)	99.1	153.4	116.4	87.2	55.4	106.1	123.5	88.5
Present-day configuration								
Grounded ice volume (m SLE)	9.0±0.1	9.5±0.3	9.1±0.3	8.7±0.3	8.7±0.2	9.0±0.4	8.55	9.08
Grounded area (10^6 km^2)	1.99±0.02	2.00±0.03	1.94±0.05	1.95±0.05	1.93±0.04	1.95±0.06	1.82	1.98
Falsely grounded (10^6 km^2)	0.19±0.01	0.21±0.02	0.17±0.03	0.18±0.03	0.17±0.03	0.18±0.04	0.07	0.19
Missing grounded (10^6 km^2)	0.08±0.01	0.08±0.01	0.11±0.02	0.11±0.02	0.12±0.02	0.10±0.02	0.13	0.08
Ice thickness RMSE† (m)	420.8	495.2	435.9	396.4	394.9	428	313.4	418.7
Bed topography RMSE (m)	27	42.2	19	18.5	17.5	20.2	58.3	58.3
Surface speed RMSE† (ma^{-1})	84.4	80.7	79.5	82.7	82	79.1	95.3	96.3
Configuration at -12 ka								
Grounded ice volume (m SLE)	15.7±0.3	16.0±0.7	15.8±0.5	15.1±0.6	15.8±0.7	15.3±0.9	9.03	14.31
Grounded area (10^6 km^2)	2.96±0.03	2.93±0.03	2.93±0.04	2.96±0.05	3.01±0.05	2.93±0.05	2.08	2.87
dvdt last 500 a (mm SLE ka^{-1})	-23±26	-31±27	-74±133	-52±106	-75±143	-60±112	-18.19	-70.81
Time of collapse (ka b2k)	4.9±0.5	4.9±0.7	6±1	6±1	5±1	6±1		
n_{eff}	9.28	41.36	151.87	99.67	28.56	841.00		

Table 2. Estimates of key observables for the past and present of the GrIS, as well as observables for the simulations restricted to the present-day Greenland mask (Grl) and the ECS. All observables are calculated within the ECS mask and do not include Canada. † RMSEs are calculated within the present-day observed grounded mask.

Figure 10 shows the modeled surface speeds and the deviations compared to Solgaard and Kusk (2023). In the northwest, the modeled ice sheet is thinner than observed at the Humboldt Glacier, where the surface speed is overestimated. In the northeast, the model fails to capture the flow of NEGIS but instead simulates a faster-flowing ice stream to the north.

Figure 11a shows the modeled present-day uplift rates, compared with GPS-derived GIA uplift rates from Schumacher et al. (2018). Figure 11b presents the difference between the modeled and observed present-day bedrock topography. Currently, the bedrock topography shows a maximum deviation of 93 m in the area covered by the IIS, with an RMSE of 27 m. Figure 11c displays the modeled bedrock uplift from -12 ka to the present, with a maximum uplift of 509 m over the IIS region. At Agassiz, the bed uplift is 345±9 m, while at Renland, it is 168±9 m. These values are slightly larger than the bed uplifts of 275 and 110 m, respectively, used by Vinther et al. (2009) for deriving the surface elevation histories.

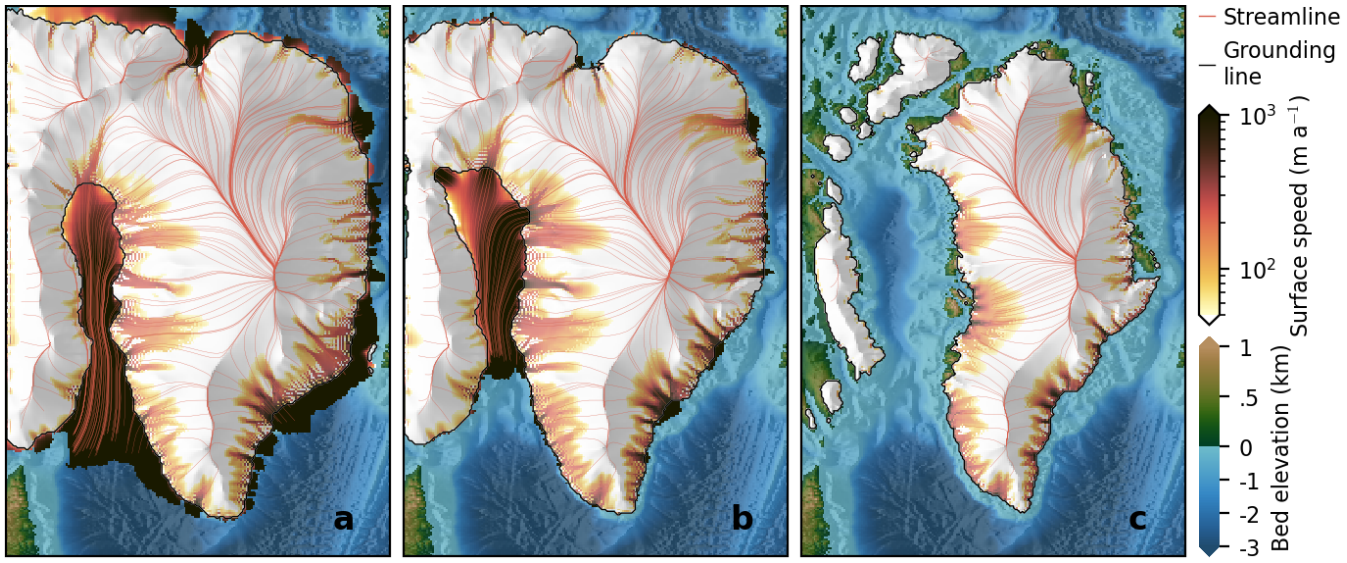

Figure 6. Time slices showing modeled surface speed, streamlines, bed topography, and ice shelf extent for the ensemble member with the highest combined likelihood at -12 ka (a), -9 ka (b), and present day (c).

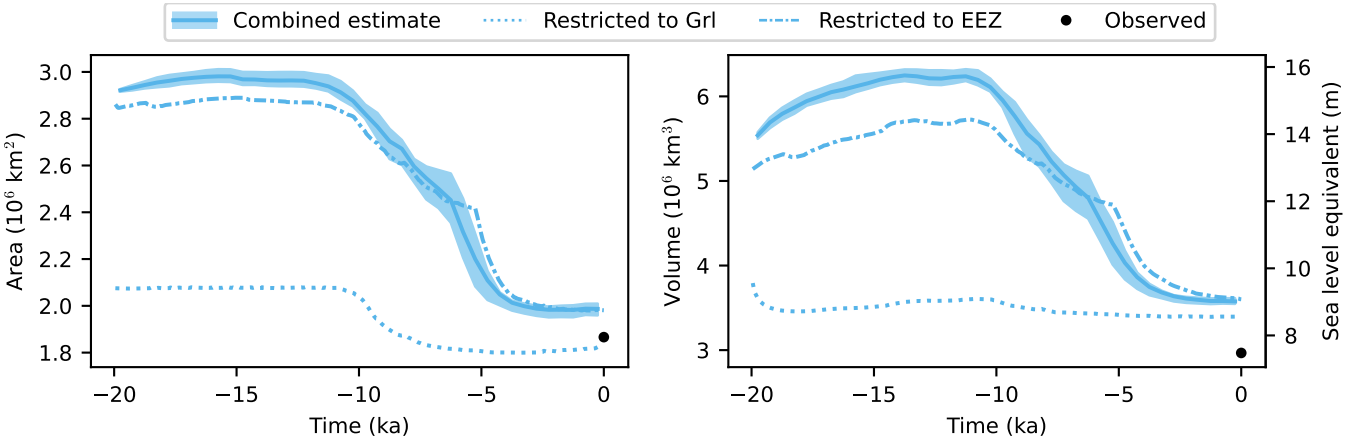

Figure 7. Modeled evolution of the GrIS grounded area (a) and volume (b). The shaded area denotes the estimated standard deviation.

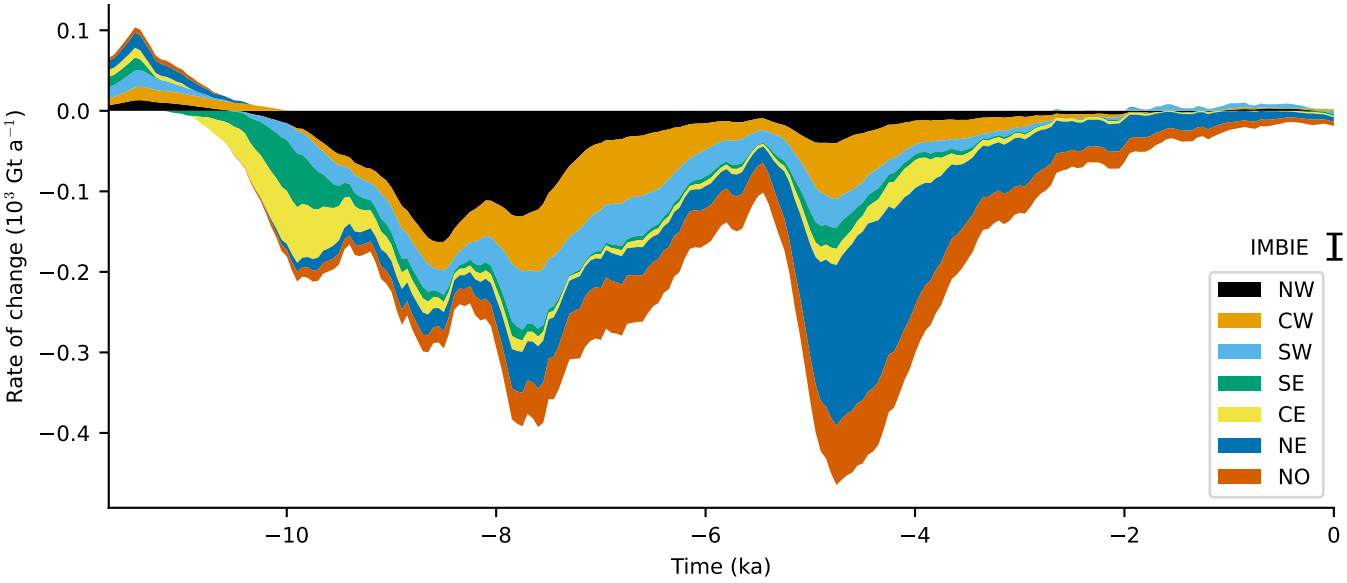

Figure 8. Rate of change of grounded ice by basin for the ensemble member with the highest likelihood. The mass change is smoothed using a running mean of 500 years, then divided into gain and loss, and then accumulated by basin. The 1992-2020 estimated mass loss rate from The IMBIE Team (2020) is shown for comparison.

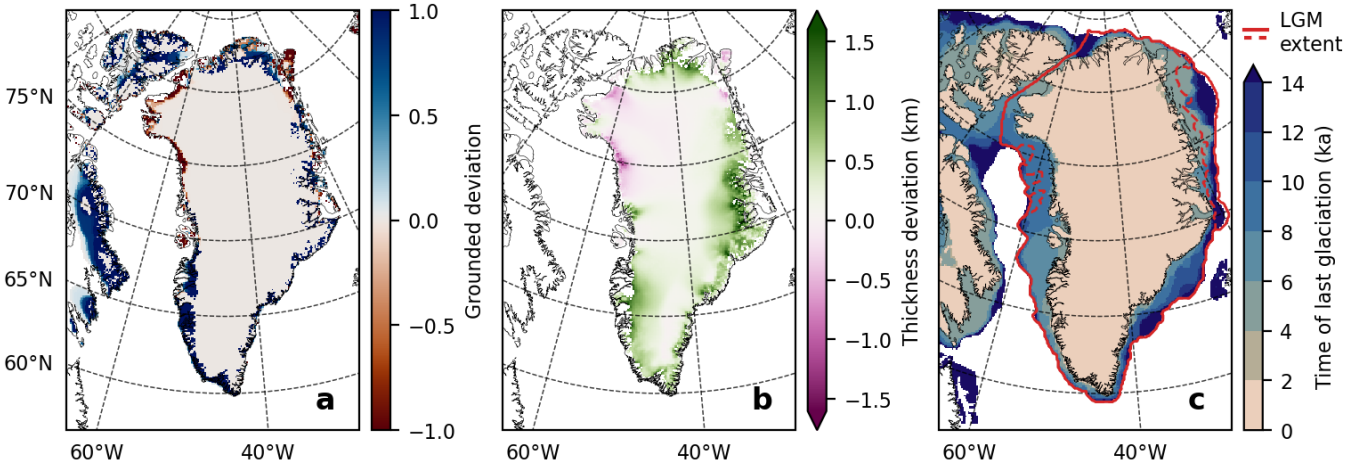

Figure 9. (a) Modeled present-day grounded extent deviation (modeled-obs) where one corresponds to grounded and zero corresponds to not grounded. (b) Modeled present-day thickness deviation from observed. (c) Isochrones showing the modeled time of the last glaciation together with the maximum (solid line) and minimum (dashed line) LGM extent from Leger et al. (2024).

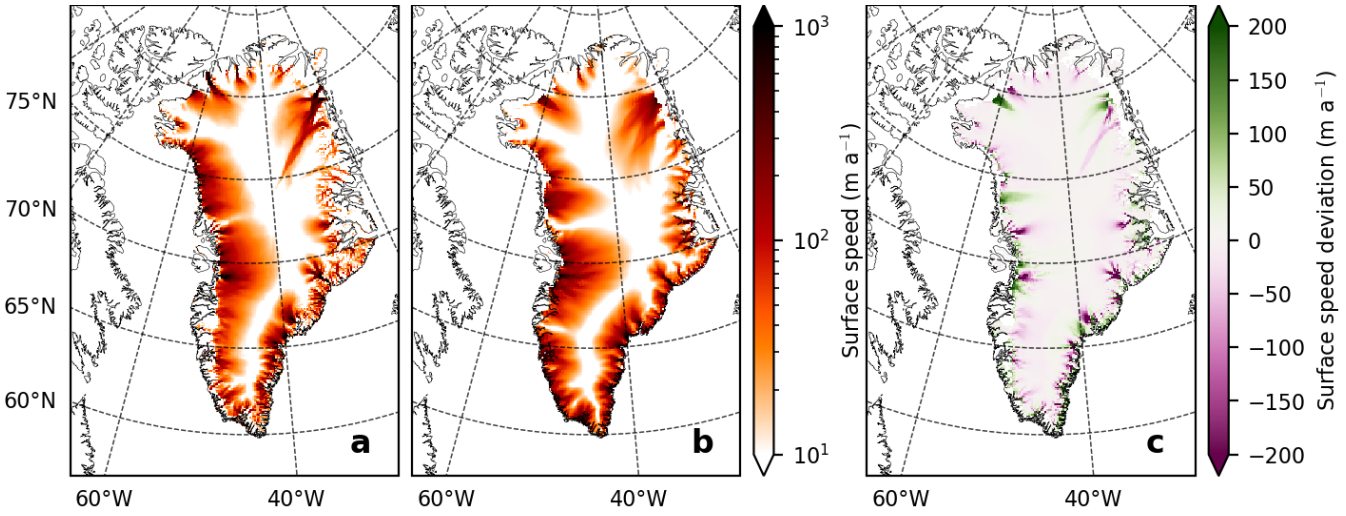

Figure 10. (a) Observed mean surface speeds over the GrIS for 2016–2022 from Solgaard et al. (2021). (b) Modeled present-day surface speeds. (c) Deviation of modeled from observed present-day surface speeds (mod - obs).

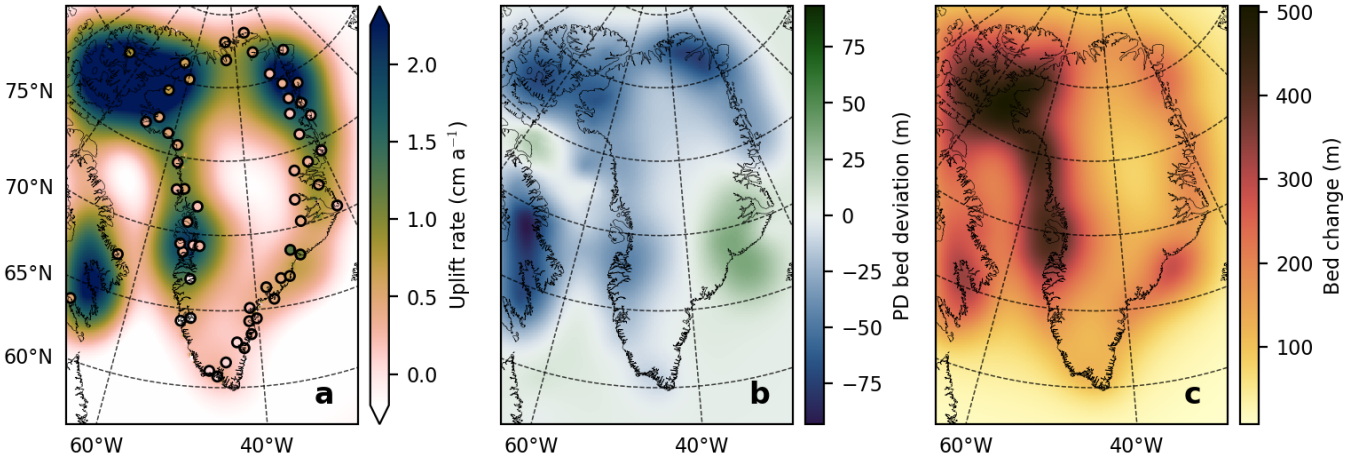

Figure 11. (a) Modeled present-day bedrock topography uplift rates and GPS-derived uplift rates from Schumacher et al. (2018). (b) Modeled present-day bedrock topography deviation from observed. (c) Modeled bed uplift between -12 ka and present-day.

6 Discussion

6.1 Innuitian ice bridge and the present-day response

To accurately model the ice-core-derived elevation history of the GrIS, we included the Canadian Arctic Archipelago in our domain and allowed the ice sheet to advance beyond present-day boundaries. These choices support the ice bridge that connected the GrIS and the IIS, as well as the ice shelf that covered Baffin Bay during the last glacial period. This, in turn, enables the ice sheet to reach sufficient thickness at the four ice-core sites before the onset of the Holocene. This is demonstrated by the two simulations constrained to the present-day land margin and the ECS.

In our model, the IIS meets the GrIS at Nares Strait during the glacial period. From the saddle point between the ice sheets, the ice then diverges into two streams: one flowing southwestward, similar to the Smith Sound Ice Stream as suggested by England et al. (2006), and another flowing northeastward. The Smith Sound Ice Stream discharges into Baffin Bay, which, as proposed by Couette et al. (2022), is covered by an extensive ice shelf that provides buttressing for the western GrIS.

Figure 9c illustrates the modeled isochrones of areas last covered by grounded ice. The modeled collapse of the ice bridge in Nares Strait occurs at 4.9±0.5 ka before present, 0.7 ka after the onset of sub-shelf melting, and about 3 ka later than the findings by England et al. (2006). The lateral retreat also occurs thousands of years later than found by Leger et al. (2024), as shown in Fig. A6.

Although not the focus of this study, it may be possible to align ice sheet evolution with both surface elevation histories and the lateral retreat and timing of the ice bridge collapse. However, ensemble members with earlier onsets of sub-shelf ocean melting, which would lead to earlier retreat, become too thin at CC in the middle of the Holocene, while those with later onsets remain too thick at present (Fig. A5). This issue might be resolved by increasing Holocene precipitation.

The importance of calibrating the GrIS evolution with paleo constraints is underscored when examining the mass change rates of the GrIS over the last 500 years. These rates range from a decrease of 487 mm ka^{-1} to an increase of 105 mm ka^{-1} across the ensemble of simulations. Excluding the simulations that utilize the temperature reconstruction from Gkinis et al. (2014), where the temperature anomaly peaks at 4.5 K during this period, we find that the remaining mass loss rates primarily depend on the timing of the onset of ocean forcing, τ (Fig. A4). This relationship exhibits a strong Pearson correlation coefficient of 0.8. Consequently, the estimated mass loss rate shifts from a prior of -12±40 mm ka^{-1} to a posterior of -23±26 mm ka^{-1}. This adjustment highlights the critical role of historical calibration in accurately modeling ice sheet dynamics.

6.2 Bedrock uplift

The present-day bedrock RMSE for the ensemble members ranges from 11.9 to 70.9 m. This is an improvement from the initial RMSE of 77.4 m before any bedrock adjustment, but it is still higher than the RMSE of 1.47 m achieved after the 12th iteration of the bedrock adjustment scheme. The discrepancy may partly arise from the bedrock adjustment being performed at a 20 km resolution, while the ensemble uses a 10 km resolution. The variation in bedrock RMSE suggests that the modeled bedrock topography is highly sensitive to the ice load history. To improve agreement between the modeled and observed present-day bedrock, additional bedrock adjustment iterations could be performed for each ensemble member, though this

would significantly increase computational demands. However, the reported error in Morlighem (2022) is up to 1000 m in the interior, where data coverage is sparse, and the RMSE is 145 m over land. Given these uncertainties, further refining the bedrock topography may provide limited improvements.

The modeled uplift rates are generally larger than the GPS-derived GIA uplift rates from Schumacher et al. (2018). This discrepancy may be due to the modeled collapse occurring too late, not allowing enough time for the bed to fully relax, or it could be because the assumed viscosity of the upper mantle is too low. A higher viscosity would result in smaller past elevation changes, leading to an earlier collapse.

The viscosity of the upper mantle was not varied in our ensemble; instead, we used the default value of 10^{21} Pa s from Lingle and Clark (1985). Estimates of viscosity vary across several orders of magnitude (Bagherbandi et al., 2022), with Albrecht et al. (2020) suggesting a plausible range of 10^{20} to 10^{22} Pa s for Antarctica. Varying the viscosity would further alter the bedrock topography history of the ensemble members, providing additional justification for adjusting the bedrock for each member individually.

6.3 Validity of elevation histories

The analysis by Vinther et al. (2009) simplifies the relationships between the O-18 content of ice, temperature, and elevation changes. It does not, however, account for the effects of an ice shelf over Baffin Bay or the influence of the IIS on the fractionation process along the moisture trajectory from the ocean to the ice core. Despite this, the derived elevation histories are supported by measurements of total gas content, which serve as an independent proxy for pressure and, consequently, for elevation at the close-off depth.

Lecavalier et al. (2013) presented revised estimates of elevation histories, arguing that the bedrock history along the eastern coastline of Ellesmere Island should be used rather than at the Agassiz location itself while arguing that the IIS complicated the elevation correction before -8 ka. Using the assumption that the elevation correction to the O-18 signal at the Agassiz ice cores should be taken from the shores, Lecavalier et al. (2017) presented revised temperature anomalies for the Agassiz ice core that, in turn, increased the ice-core-derived surface elevation at CC by 400 m at the Holocene onset.

The elevation histories from Vinther et al. (2009) are already corrected for upstream effects due to ice flow. Ideally, the ice sheet model should be coupled with an atmospheric model that tracks moisture from ocean evaporation to ice sheet precipitation and O-18 fractionation. The modeled O-18 should then be compared directly with the observed values at the time-dependent ice core site location.

The assumption that the thickness of the Renland ice cap remains constant throughout the Holocene contradicts our model results. We find that the Renland ice cap thins by 399 ± 56 m from the Holocene onset to present day. This discrepancy may be due to the low resolution of our model, as the Renland ice cap covers only 1200 km^2 (Johnsen et al., 1992), and the model cannot capture the steep descents in topography that limit its lateral extent.

6.4 Sampling technique

We applied the second-order orthogonal Latin Hypercube Sampling (LHS) technique to efficiently explore the 20 unknown model parameters critical for modeling the ice-core-derived surface elevation histories. This sampling strategy was selected for its ability to cover the high-dimensional parameter space more uniformly than simple random sampling, reducing errors in the estimation process. The effective sample size of the combined estimate is 9.28, indicating that the weight is concentrated among a few samples, with the two most likely members contributing 42% to the estimates. To improve this, an adaptive sampling technique could be implemented, which focuses sampling density on the regions of the parameter space that most influence the estimates. We only performed this adaptively in an ad-hoc way, with the sample ranges outlined in Table 1.

6.5 Inferred parameters

The modeled evolution of the ice sheet during the Holocene is influenced by multiple model parameters, which may compensate for each other due to the complexity of the dynamic processes and climate forcings involved. As a result, interactions between these parameters can obscure their individual effects, making it difficult to draw definitive conclusions from the inferred parameter PDFs.

Nonetheless, differences in the PDFs across the four ice core sites suggest spatial variations that our model does not capture. For instance, the surface elevation history at Dye 3 in the south favors reconstructions with a warm Holocene Thermal Maximum, while CC in the north favors a colder Holocene climate. This could indicate regional temperature differences that challenge the assumption by Vinther et al. (2009) that local temperature offsets were solely due to a uniform, Greenland-wide anomaly and elevation feedback. However, these differences might also reflect compensations for other spatial factors, such as variations in ice rheology or basal friction.

The differences in the estimated ice flow parameters may also be attributed to the poorly resolved outlet glaciers, which lead to a lower ice flux. This is often compensated by increasing the enhancement factors. Notably, both Kangerlussuaq Gletscher in eastern Greenland and Sermeq Kujalleq in western Greenland require a resolution of less than 3.6 km to be properly resolved, as suggested by Aschwanden et al. (2016), which is not feasible for this study. Additionally, it is possible that the ice-core-derived surface elevation records do not provide sufficient constraints for all model parameters.

6.6 Climatic forcing

The atmospheric conditions and spatial patterns of temperature and precipitation during the glacial and the early Holocene were possibly quite different from that of present day. The Laurentide Ice Sheet is thought to have both shielded Ellesmere Island from precipitation and, at the same time, deflected the jet stream such that more moisture was transported north of the Laurentide Ice Sheet from the North Pacific Ocean to the Polar regions, making the amount of precipitation over Greenland uncertain (England et al., 2006). Furthermore, the ice shelf at Baffin Bay has likely affected the temperature and precipitation non-uniformly. Fully coupling the ice sheet to the atmosphere and ocean could provide a more detailed understanding of this effect.

We also tried to use the temperature anomalies from Lecavalier et al. (2017) but found that although it did give an elevation change that was similar to the ice-core-derived, the modeled present-day elevation was far too low with the ice sheet retreating far inland in the northwest.

Our model adopts a simplified approach to ocean forcing, reflecting the limited knowledge of its history and improving interpretability. As discussed above, the inferred onset of ocean forcing at -5.6±0.6 ka must occur this early to prevent the ice sheet from becoming too thin at CC during the mid-Holocene. Once this issue is addressed, it may be possible to constrain the model to the lateral retreat reconstructed by Leger et al. (2024) by introducing different onset timings for the western and eastern regions of Greenland. This approach could then provide further insights into ocean forcing.

6.7 Uniform temperature anomalies

Our choice to use uniform temperature anomalies to force the model aligns with the assumption of Vinther et al. (2009) that local temperature offsets were due to a Greenland-wide temperature anomaly and local elevation feedback. Non-uniform temperature anomaly products do exist, such as the TraCE-21K climate simulations (Liu et al., 2009) and the derivative product of Badgeley et al. (2020), which was assimilated to match ice-core-derived temperatures. However, we believe it is best practice to avoid using these products, as they were simulated using the topography of ICE-5G (Peltier, 2004). This ensures that our ice sheet reconstruction remains independent of previous reconstructions and avoids circular assumptions.

6.8 Holocene evolution and ice mass loss

In our simulations, the ice sheet begins to thin and retreat in response to the temperature rise in the early Holocene, prior to the onset of ocean forcing. This leads to the collapse of the ice shelf in Baffin Bay, reducing buttressing and causing further retreat of the ice sheet. After ocean forcing begins, mass loss accelerates, as shown in Fig. 8, and the ice bridge at Nares Strait collapses.

Overall, our simulations show that the deglaciation in Greenland occurred between around 10 ka and 3.5 ka, where the total area and volume of the GrIS dramatically decreased from its glacial maximum values to approximately the present-day volume and extent (Fig. 7). The minimum ice-covered area occurred approximately at -2 ka and slightly increased towards the present, while the ice volume has remained relatively constant over the last millennia. Our simulation shows no clear evidence of a minimum ice volume during the Holocene Thermal Maximum. It ends at the present day with a simulated area and volume that exceed the observed values by 5.9% and 20.5%, respectively (Fig. 7).

A previous study by Nielsen et al. (2018) showed that the evolution of the GrIS depends on the assumed climate history through the Holocene. Nielsen et al. (2018) found that the GrIS retreated to a smaller than present-day volume at around 8 ka ago when forced by temperature anomalies that contain the Holocene Thermal Maximum, but their simulations did not include Canada in the domain, and thus initiated their simulation with a GrIS of similar size as at present day. In our simulations, we used the same climate forcing histories as in the study by Nielsen et al. (2018), but we do not find a similar minimum in our simulations for the ensemble members that include the Holocene Thermal Maximum, most likely because the GrIS is too far from equilibrium during the Holocene Thermal Maximum due to the large initial ice sheet. In fact, the simulations that best

fit all surface elevation histories are those forced with the climate reconstruction history number 1 (see Fig. 5), which did not show any Holocene Thermal Maximum. For this climate reconstruction, our simulated Holocene ice volume follows a similar pattern as found in Nielsen et al. (2018).

The spatial pattern of mass loss rates from the GrIS has shifted significantly during the Holocene (Fig. 8). In the earliest part of the Holocene, the rate of mass change was slightly positive in all basins due to an increase in snow accumulation over the GrIS. During the first deglaciation phase between 10 and 5.5 ka ago, the mass loss rate was large in all basins, with the largest mass loss rate in the northwest basin, being about the same rate as all other basins combined. The central west basin also had significant mass loss rates, followed by the north and southwest basins. Towards 5.5 ka, the mass loss rates decreased towards zero, which is also seen in the volume record as a temporary stabilization. Between 5.5 ka and 3.5 ka, after the onset of the sub-shelf melt, a second phase in the deglaciation occurred, with a total higher mass loss rate than the first phase, and now dominated by high mass loss rates from the northeast basin and to a lesser extent from the north and central west basins. These two deglaciation phases are also seen in the total volume (Fig. 7b), with a kink around 5.5 ka ago separating the two phases.

Our simulated Holocene mass loss rates exceed the mass loss rates estimated in a previous study (Briner et al., 2020). Briner et al. (2020) simulated the Holocene evolution of the CW and SW basins and assumed that regions are representative of the entire GrIS. They found the maximal values of mass loss during the Holocene to be 60 Gt a^{-1} and that it would most likely be exceeded within this century with rates of mass loss of 8.8 to 359 Gt a^{-1} depending on the climate scenario which is less than our maximal Holocene rate of mass loss at 548 Gt a^{-1} for the ensemble member with the highest likelihood. Our results show that the spatial pattern of retreat has shifted geographically during the Holocene, and the mass loss rates from the GrIS basins have peaked thousands of years earlier in the northwest and west than in the northeast. We conclude that one basin cannot be representative of the entire GrIS, and thus, our results are not directly comparable to the results by Briner et al. (2020).

7 Conclusions

We considered an ensemble of ice sheet model simulations covering both Greenland and the Canadian Arctic Archipelago through the Holocene. In these simulations, we varied 20 key parameters to constrain the ice sheet evolution to ice-core-derived surface elevation histories at four ice-core sites in Greenland. We showed that the inclusion of Canada in the model domain and the ability of the ice sheet to advance beyond the present-day land margin are necessary for accurately modeling the ice-core-derived elevation history.

We found that during the last glacial period, the GrIS was connected to the IIS with an ice bridge over Nares Strait. Within the Extended Continental Shelf (ECS), the GrIS had an extent that was 49% larger than the present-day modeled area 12 ka ago, and it was found to have contributed 5.3$\pm$0.3 m SLE to the global mean sea level from 12 ka ago to present day. The collapse of the ice bridge at Nares Strait was found to have occurred at 4.9$\pm$0.5 ka before the present.

We show that the present mass loss rate is a combined short-term response to the recent climate forcing and long-term dynamical response on millennia timescales due to the deglaciation history. Ignoring outliers with excessive temperature anomalies over the past half-millennium, we find that the mass loss rates over the last 500 years primarily depend on the timing of the

onset of ocean forcing during the deglaciation. Bayesian inference modifies our understanding of the previous 500 years' mass loss from a prior estimation of 12 ± 40 mm ka^{-1} to a posterior of 23 ± 26 mm ka^{-1}, which is about 5% of the 1992-2020 estimated mass loss rate (The IMBIE Team, 2020) and 7% of the estimated 21st-century committed mass loss rate (Nias et al., 2023). This adjustment underscores the significance of historical calibration in accurately modeling ice sheet behavior and including its long-term response to past climatic changes.

While our study was able to model the ice-core derived surface elevation histories, the most probable ice sheet simulations did not match the timing of the ice bridge collapse found by England et al. (2006) or the timing of the retreat found by Leger et al. (2024). We propose that these geologically derived datings could be added as further constraints to the GrIS Holocene evolution in future simulations. This would help reveal limitations in the model and assess the sensitivity of model parameters. We also found that our modeled present-day uplift rates deviated from the GPS-derived uplift rates in northwest Greenland, which is further in line with the timing of our model collapse happening too late. In future studies, these deviations should be used to constrain the mantle viscosity in tandem with accurately determining the timing of the retreat. Overall, our results show that the present-day GrIS still responds to the history of deglaciation. This long-term dynamical response is significant and should be included in studies of the present and future mass loss from the GrIS.

Code and data availability. PISM is an open source software that can be downloaded from github.com/pism/pism (Bueler and Brown, 2009; Winkelmann et al., 2011). Surface elevation data from the four ice core locations are available upon request. The presented RACMO data are available upon request and without conditions from B. Noël (bnoel@uliege.be). Temperature reconstructions can be downloaded from iceandclimate.nbi.ku.dk/data/.

Video supplement. A video showing the GrIS evolution through the Holocene for the most likely ensemble member can be found at doi.org/10.5446/68337

Appendix A

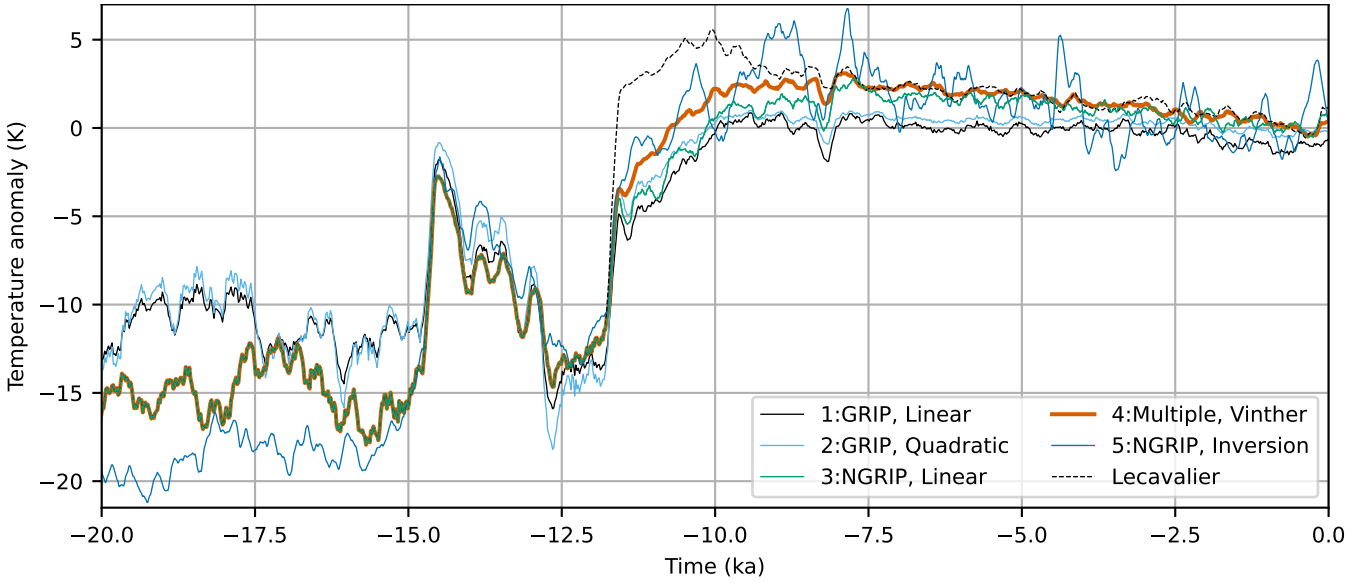

Figure A1. Paleoclimatic temperature anomalies derived from O-18 measurements at GRIP and NGRIP using linear transfer function (Huybrechts, 2002) and quadratic transfer function from Johnsen et al. (1995) and O-18 measurements at Renland and Agassiz (Vinther et al., 2009) and O-18 measurements at NGRIP using an inversion scheme (Gkinis et al., 2014).

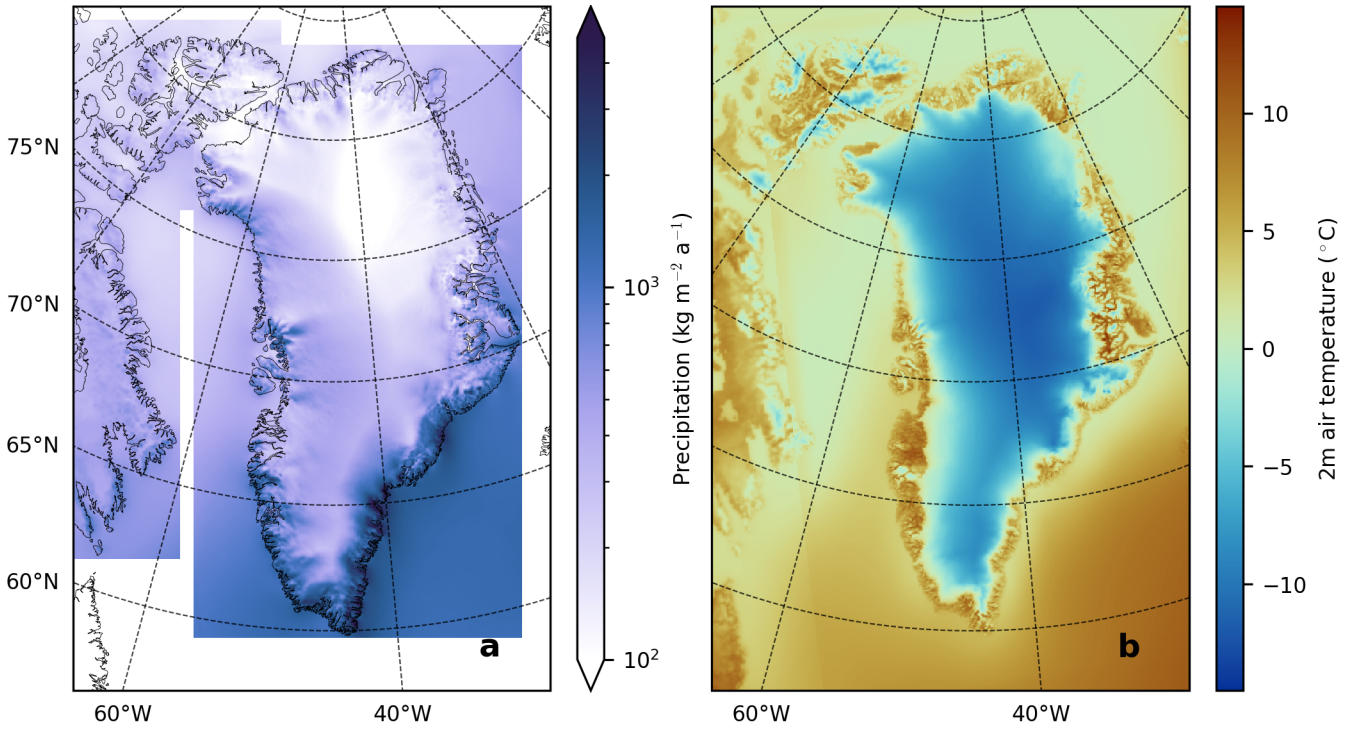

Figure A2. (a) Annual mean precipitation and (b) summer (June, July, and August) mean 2 m temperatures for our 30-year reference climatology (1960-1989).

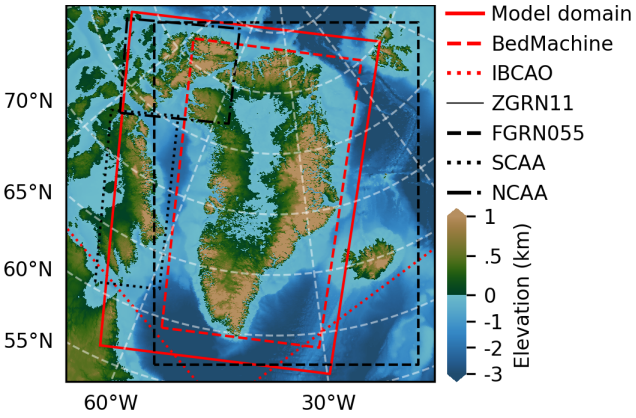

Figure A3. Overview of different domain boundaries used to patch together the 30-year reference climatology (ZGRN11, FGRN055, SCAA, NCAA) and the bedrock topography (BedMachine, IBCAO, GEBCO).

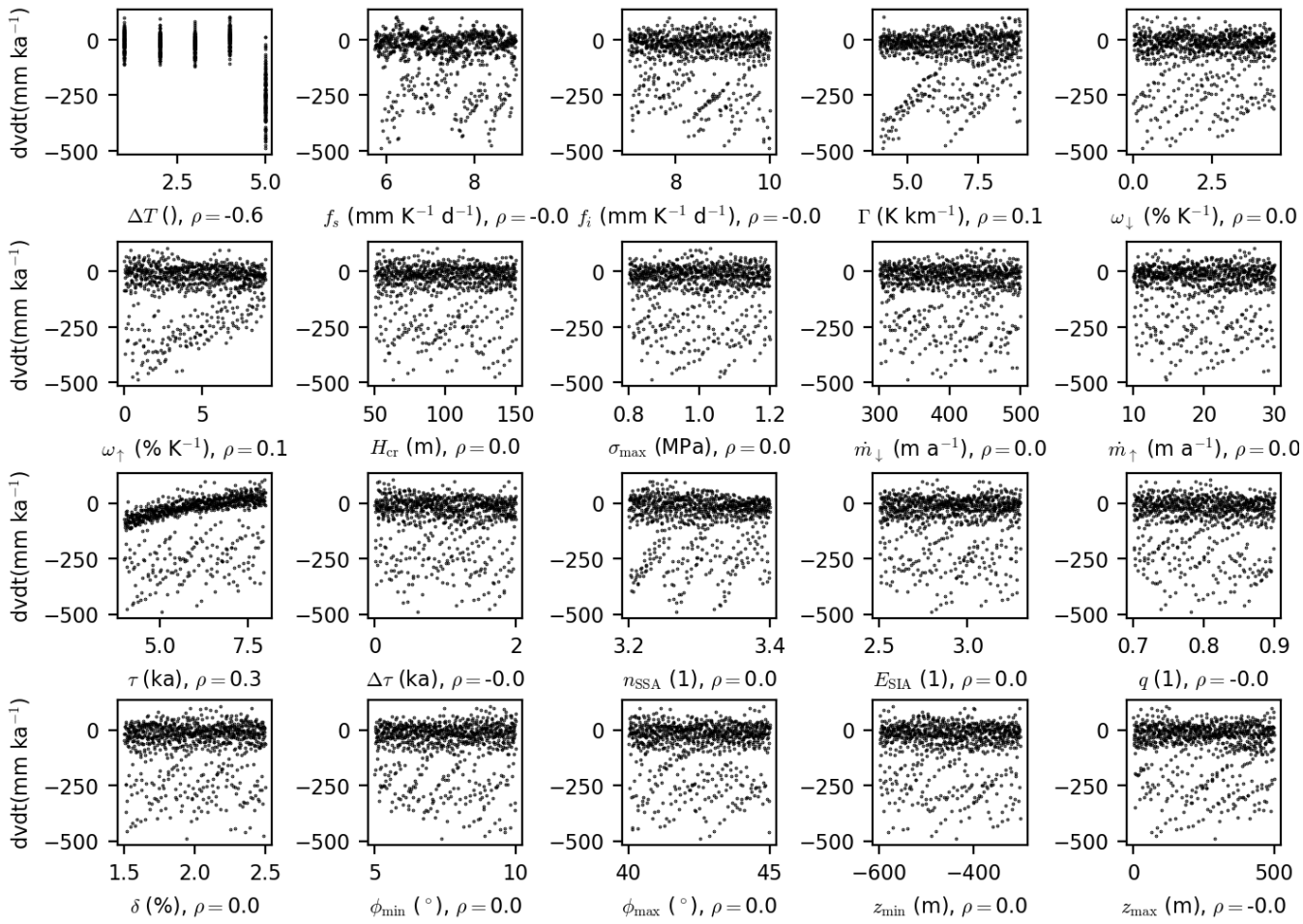

Figure A4. Scatterplot of the last 500 years of mass loss rates vs each parameter varied in our ensemble. ρ is the Pearson correlation.

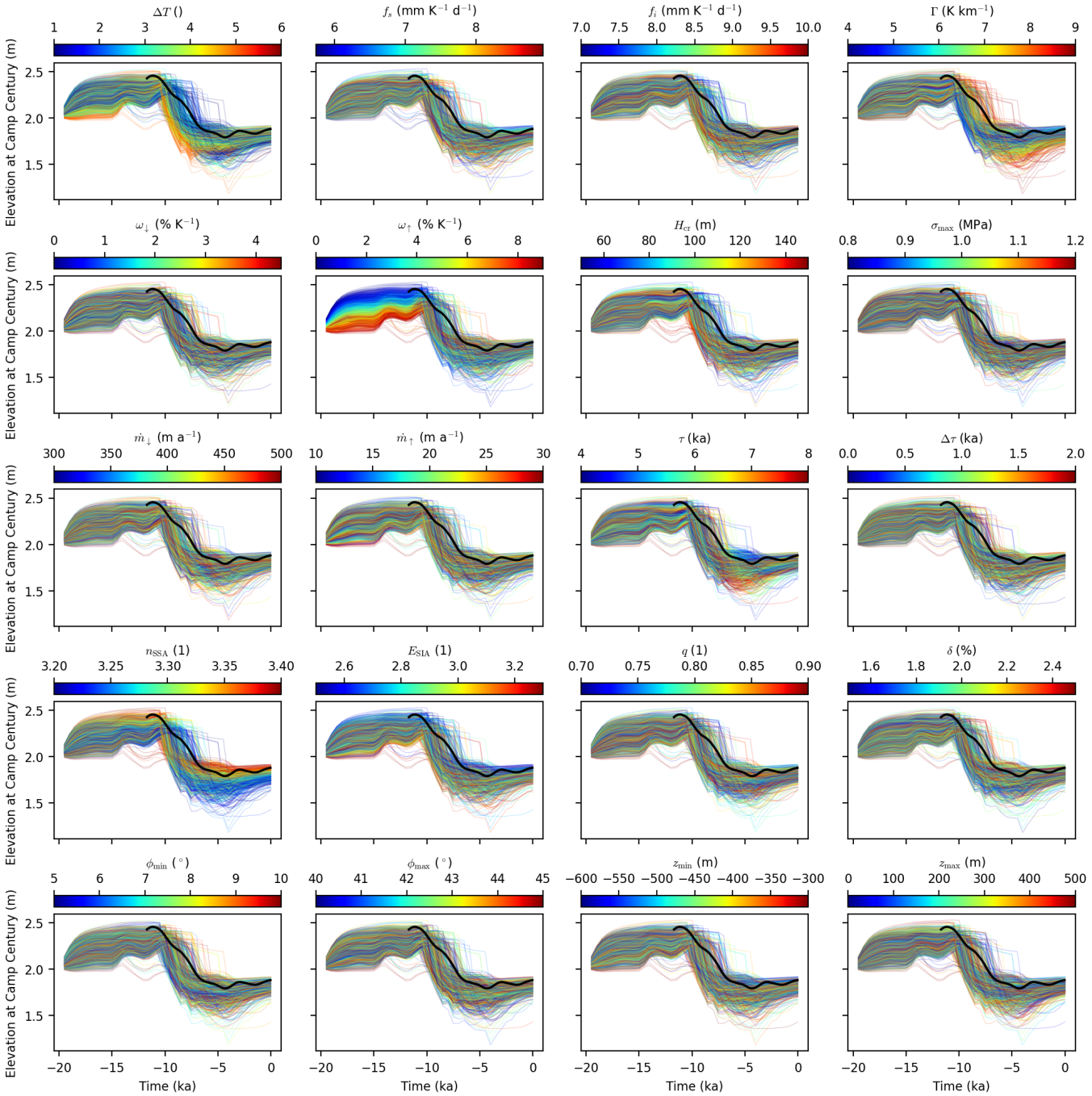

Figure A5. Modeled surface elevation at Camp Century color coded for each parameter.

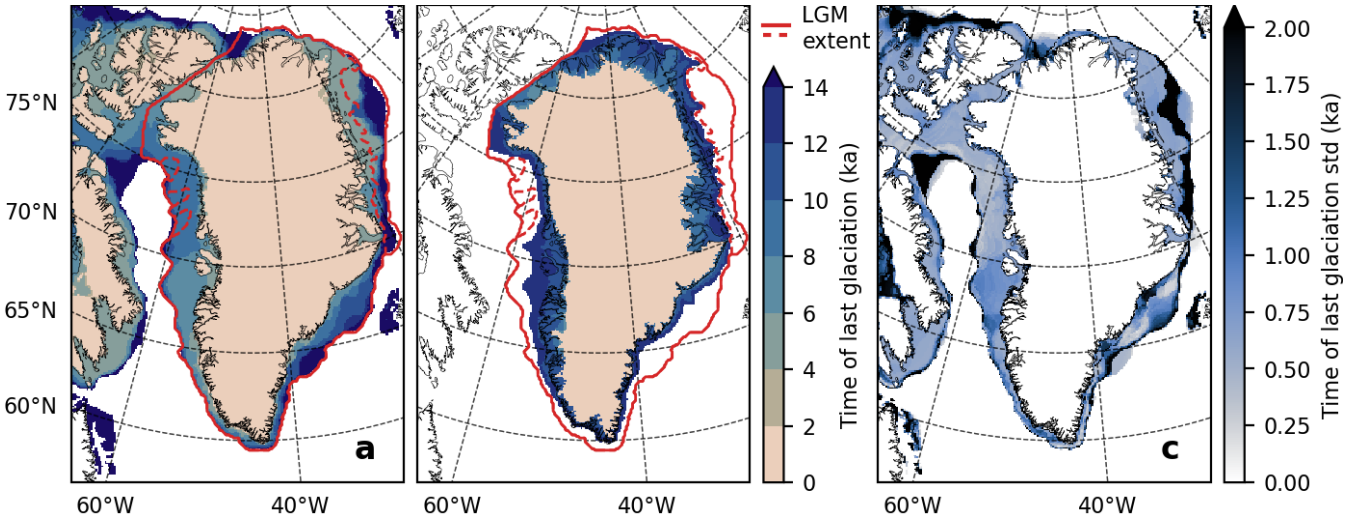

Figure A6. Isochrones showing the time of last glaciation for the model (a) and for the empirical reconstruction of Leger et al. (2024) (b). The red lines mark the maximum (solid) and minimum (dashed) LGM extent from Leger et al. (2024). (c) shows the modeled standard deviation of the time of last glaciation.

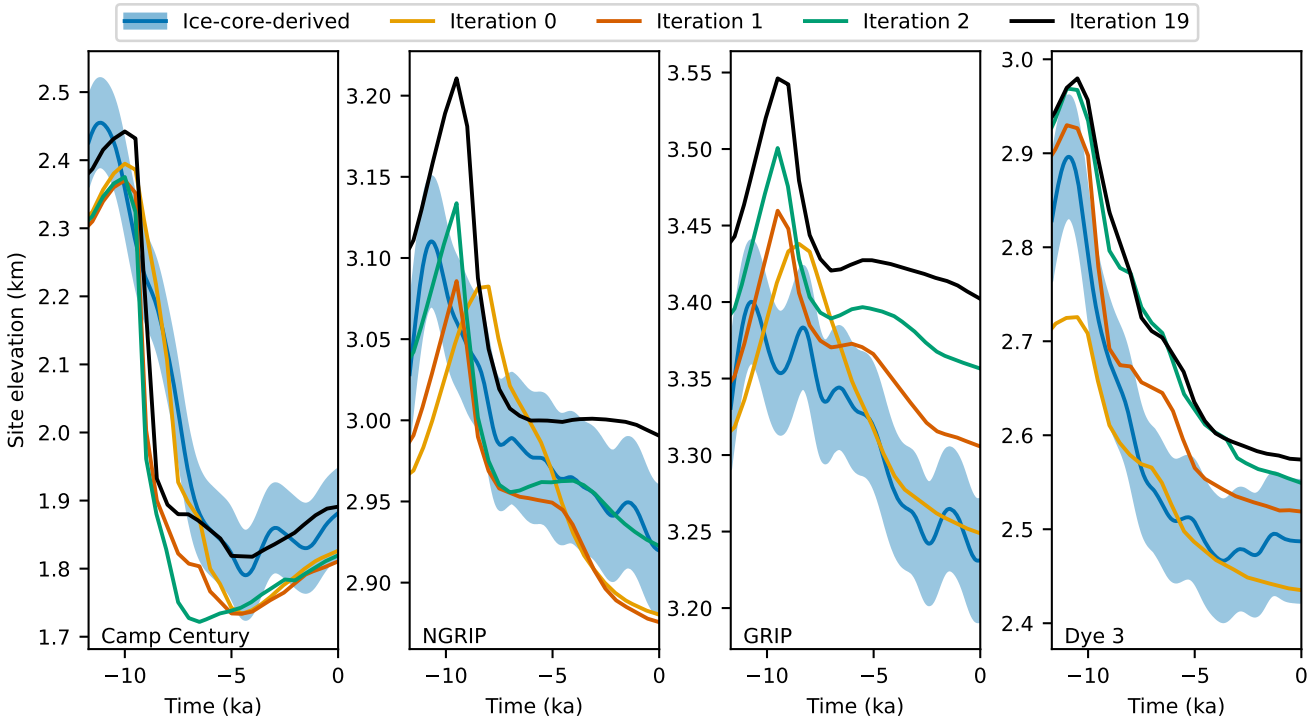

Figure A7. Observed and modeled surface elevation over the past 11.7 ka at the ice core sites Camp Century, NGRIP, GRIP, and Dye 3. The blue lines represent ice-core-derived surface elevations from Vinther et al. (2009), with the blue envelopes indicating one standard deviation. The orange, red, green, and black lines correspond to the modeled surface elevations for the 0th, 1st, 2nd, and 19th iterations of the bedrock adjustment, respectively.

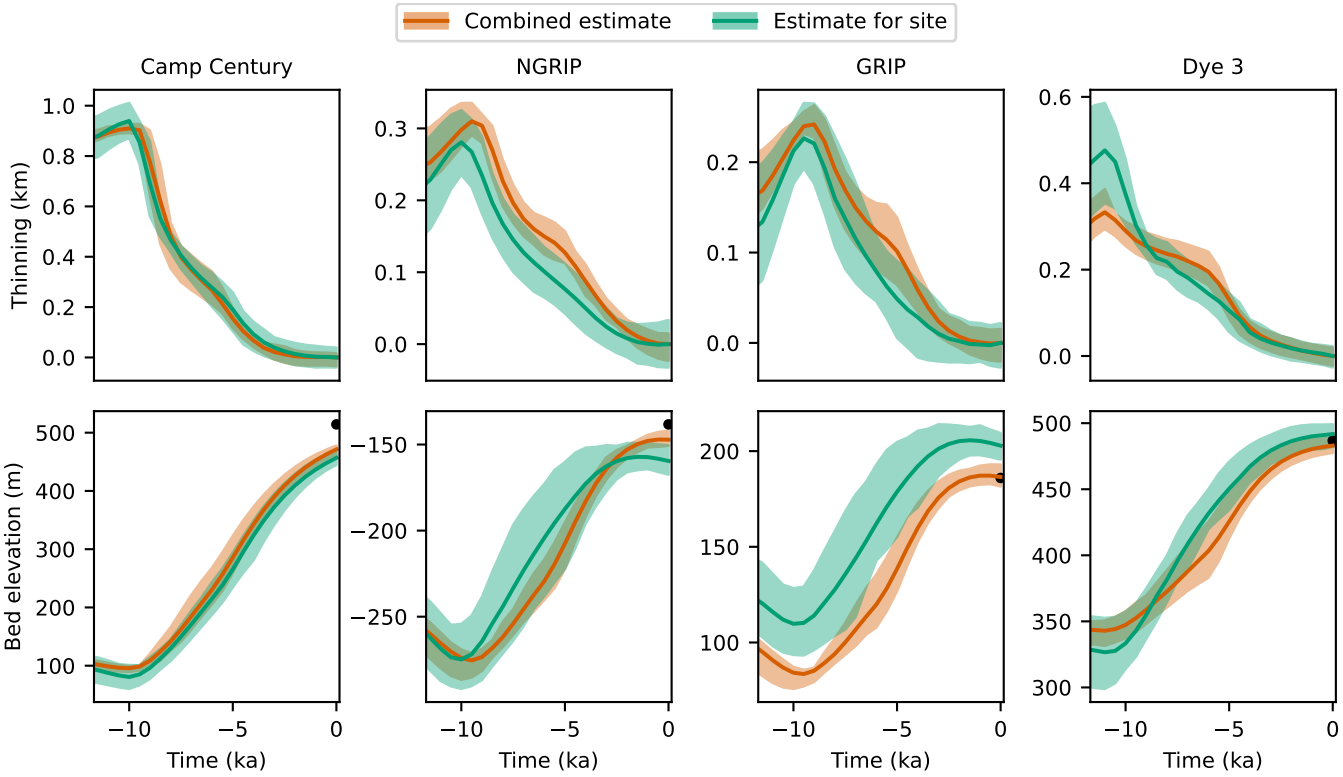

Figure A8. Modeled bedrock elevation and thinning over the past 11.7 ka at the ice core sites Camp Century, NGRIP, GRIP, and Dye 3. The red envelopes represent the ensemble-estimated mean and standard deviation, while the green envelopes show the site-specific estimate. The black dots indicate the observed present-day bedrock elevation from Morlighem et al. (2017).

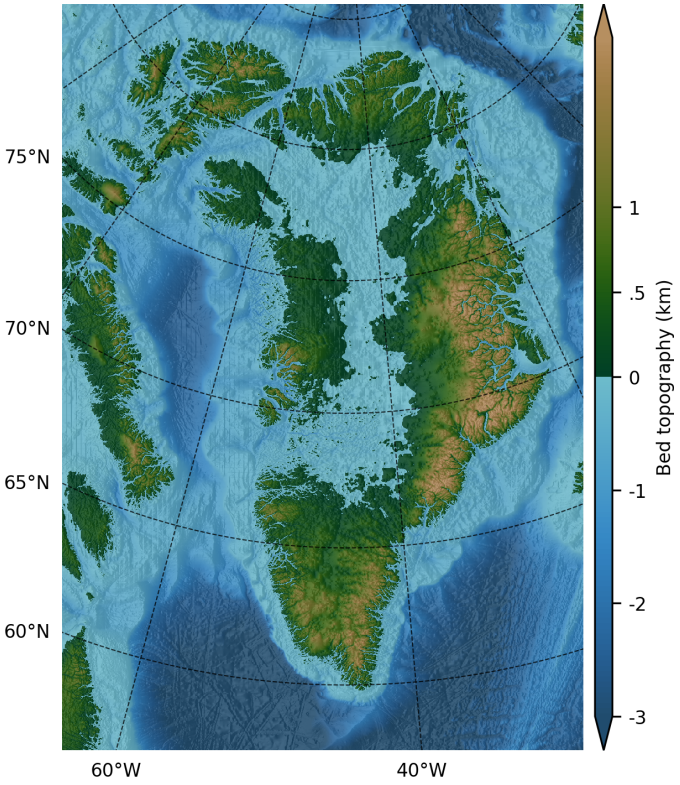

Figure A9. Bedrock topography at -20 ka, which results in the smallest deviation from present-day observed bedrock topography. This topography is used at -20 ka for all ensemble members.

Author contributions. ML, CH, and AS designed the study. ML prepared the data, performed the model runs, and carried out the subsequent analysis. All authors discussed and improved the paper.

Competing interests. The authors declare that they have no conflict of interest.

Acknowledgements. ML was funded by the Independent Research Fund Denmark through the project GreenPlanning, grant no. 0217-00244B. CH, NR, and AG received funding from the Novo Nordisk Foundation, grant no. NNF23OC0081251, the Independent Research Fund Denmark (DFF), grant no. 2032-00364B, and the Villum Foundation, grant no. 23261. BN is a Research Associate of the Fonds de la Recherche Scientifique de Belgique – F.R.S.-FNRS We would also like to thank Benoit Lecavalier for providing the temperature anomalies derived from the Agassiz ice core in Lecavalier et al. (2017).

References

Aðalgeirsdóttir, G., Aschwanden, A., Khroulev, C., Boberg, F., Mottram, R., Lucas-Picher, P., and Christensen, J.: Role of Model Initialization for Projections of 21st-Century Greenland Ice Sheet Mass Loss, Journal of Glaciology, 60, 782–794, https://doi.org/10.3189/2014JoG13J202, 2014.

Albrecht, T., Winkelmann, R., and Levermann, A.: Glacial-Cycle Simulations of the Antarctic Ice Sheet with the Parallel Ice Sheet Model (PISM) – Part 2: Parameter Ensemble Analysis, The Cryosphere, 14, 633–656, https://doi.org/10.5194/tc-14-633-2020, 2020.

Andersen, K. K., Azuma, N., Barnola, J.-M., Bigler, M., Biscaye, P., Caillon, N., Chappellaz, J., Clausen, H. B., Dahl-Jensen, D., Fischer, H., Flückiger, J., Fritzsche, D., Fujii, Y., Goto-Azuma, K., Grønvold, K., Gundestrup, N. S., Hansson, M., Huber, C., Hvidberg, C. S., Johnsen, S. J., Jonsell, U., Jouzel, J., Kipfstuhl, S., Landais, A., Leuenberger, M., Lorrain, R., Masson-Delmotte, V., Miller, H., Motoyama, H., Narita, H., Popp, T., Rasmussen, S. O., Raynaud, D., Rothlisberger, R., Ruth, U., Samyn, D., Schwander, J., Shoji, H., Siggard-Andersen, M.-L., Steffensen, J. P., Stocker, T., Sveinbjörnsdóttir, A. E., Svensson, A., Takata, M., Tison, J.-L., Thorsteinsson, Th., Watanabe, O., Wilhelms, F., White, J. W. C., and North Greenland Ice Core Project members: High-Resolution Record of Northern Hemisphere Climate Extending into the Last Interglacial Period, Nature, 431, 147–151, https://doi.org/10.1038/nature02805, 2004.

Aschwanden, A. and Brinkerhoff, D. J.: Calibrated Mass Loss Predictions for the Greenland Ice Sheet, Geophysical Research Letters, 49, e2022GL099 058, https://doi.org/10.1029/2022GL099058, 2022.

Aschwanden, A., Fahnestock, M. A., and Truffer, M.: Complex Greenland Outlet Glacier Flow Captured, Nature Communications, 7, 10 524, https://doi.org/10.1038/ncomms10524, 2016.

Aschwanden, A., Fahnestock, M. A., Truffer, M., Brinkerhoff, D. J., Hock, R., Khroulev, C., Mottram, R., and Khan, S. A.: Contribution of the Greenland Ice Sheet to Sea Level over the next Millennium, Science Advances, 5, eaav9396, https://doi.org/10.1126/sciadv.aav9396, 2019.

Aschwanden, A., Bartholomaus, T. C., Brinkerhoff, D. J., and Truffer, M.: Brief Communication: A Roadmap towards Credible Projections of Ice Sheet Contribution to Sea Level, The Cryosphere, 15, 5705–5715, https://doi.org/10.5194/tc-15-5705-2021, 2021.

Badgeley, J. A., Steig, E. J., Hakim, G. J., and Fudge, T. J.: Greenland Temperature and Precipitation over the Last 20 000 Years Using Data Assimilation, Climate of the Past, 16, 1325–1346, https://doi.org/10.5194/cp-16-1325-2020, 2020.

Bagherbandi, M., Amin, H., Wang, L., and Shirazian, M.: Mantle Viscosity Derived From Geoid and Different Land Uplift Data in Greenland, Journal of Geophysical Research: Solid Earth, 127, e2021JB023 351, https://doi.org/10.1029/2021JB023351, 2022.

Bindschadler, R. A., Nowicki, S., Abe-Ouchi, A., Aschwanden, A., Choi, H., Fastook, J., Granzow, G., Greve, R., Gutowski, G., Herzfeld, U., Jackson, C., Johnson, J., Khroulev, C., Levermann, A., Lipscomb, W. H., Martin, M. A., Morlighem, M., Parizek, B. R., Pollard, D., Price, S. F., Ren, D., Saito, F., Sato, T., Seddik, H., Seroussi, H., Takahashi, K., Walker, R., and Wang, W. L.: Ice-Sheet Model Sensitivities to Environmental Forcing and Their Use in Projecting Future Sea Level (the SeaRISE Project), Journal of Glaciology, 59, 195–224, https://doi.org/10.3189/2013JoG12J125, 2013.

Braithwaite, R. J.: Calculation of Degree-Days for Glacier-Climate Research, Zeitschrift für Gletscherkunde und Glazialgeologie, 20/1984, 1–8, 1985.

Briner, J. P., Cuzzone, J. K., Badgeley, J. A., Young, N. E., Steig, E. J., Morlighem, M., Schlegel, N.-J., Hakim, G. J., Schaefer, J. M., Johnson, J. V., Lesnek, A. J., Thomas, E. K., Allan, E., Bennike, O., Cluett, A. A., Csatho, B., De Vernal, A., Downs, J., Larour, E., and Nowicki, S.: Rate of Mass Loss from the Greenland Ice Sheet Will Exceed Holocene Values This Century, Nature, 586, 70–74, https://doi.org/10.1038/s41586-020-2742-6, 2020.

Bueler, E. and Brown, J.: Shallow Shelf Approximation as a "Sliding Law" in a Thermomechanically Coupled Ice Sheet Model, Journal of Geophysical Research, 114, F03 008, https://doi.org/10.1029/2008JF001179, 2009.

Bueler, E. and van Pelt, W.: Mass-Conserving Subglacial Hydrology in the Parallel Ice Sheet Model Version 0.6, Geoscientific Model Development, 8, 1613–1635, https://doi.org/10.5194/gmd-8-1613-2015, 2015.

Bueler, E., Lingle, C. S., and Brown, J.: Fast Computation of a Viscoelastic Deformable Earth Model for Ice-Sheet Simulations, Annals of Glaciology, 46, 97–105, https://doi.org/10.3189/172756407782871567, 2007.

Clark, P. U., He, F., Golledge, N. R., Mitrovica, J. X., Dutton, A., Hoffman, J. S., and Dendy, S.: Oceanic Forcing of Penultimate Deglacial and Last Interglacial Sea-Level Rise, Nature, 577, 660–664, https://doi.org/10.1038/s41586-020-1931-7, 2020.

Couette, P.-O., Lajeunesse, P., Ghienne, J.-F., Dorschel, B., Gebhardt, C., Hebbeln, D., and Brouard, E.: Evidence for an Extensive Ice Shelf in Northern Baffin Bay during the Last Glacial Maximum, Communications Earth & Environment, 3, 225, https://doi.org/10.1038/s43247-022-00559-7, 2022.

Dansgaard, W., Johnsen, S. J., Møller, J., and Langway, C. C.: One Thousand Centuries of Climatic Record from Camp Century on the Greenland Ice Sheet, Science, 166, 377–381, https://doi.org/10.1126/science.166.3903.377, 1969.

England, J., Atkinson, N., Bednarski, J., Dyke, A., Hodgson, D., and Ó Cofaigh, C.: The Innuitian Ice Sheet: Configuration, Dynamics and Chronology, Quaternary Science Reviews, 25, 689–703, https://doi.org/10.1016/j.quascirev.2005.08.007, 2006.

Eyring, V., Gillett, N., Achuta Rao, K., Barimalala, R., Barreiro Parrillo, M., Bellouin, N., Cassou, C., Durack, P., Kosaka, Y., McGregor, S., Min, S., Morgenstern, O., and Sun, Y.: Human Influence on the Climate System, in: Climate Change 2021: The Physical Science Basis. Contribution of Working Group I to the Sixth Assessment Report of the Intergovernmental Panel on Climate Change, edited by Masson-Delmotte, V., Zhai, P., Pirani, A., Connors, S., Péan, C., Berger, S., Caud, N., Chen, Y., Goldfarb, L., Gomis, M., Huang, M., Leitzell, K., Lonnoy, E., Matthews, J., Maycock, T., Waterfield, T., Yelekçi, O., Yu, R., and Zhou, B., pp. 423–552, Cambridge University Press, Cambridge, United Kingdom and New York, NY, USA, https://doi.org/10.1017/9781009157896.005, 2021.

Flanders Marine Institute (VLIZ), Belgium: Maritime Boundaries Geodatabase: Maritime Boundaries and Exclusive Economic Zones (200NM), Version 12, https://doi.org/10.14284/632, 2023.

Franke, S., Bons, P. D., Westhoff, J., Weikusat, I., Binder, T., Streng, K., Steinhage, D., Helm, V., Eisen, O., Paden, J. D., Eagles, G., and Jansen, D.: Holocene Ice-Stream Shutdown and Drainage Basin Reconfiguration in Northeast Greenland, Nature Geoscience, 15, 995–1001, https://doi.org/10.1038/s41561-022-01082-2, publisher: Nature Publishing Group, 2022.

GEBCO Bathymetric Compilation Group: The GEBCO_2023 Grid - a Continuous Terrain Model of the Global Oceans and Land., https://doi.org/10.5285/F98B053B-0CBC-6C23-E053-6C86ABC0AF7B, 2023.

Gkinis, V., Simonsen, S., Buchardt, S., White, J., and Vinther, B.: Water Isotope Diffusion Rates from the NorthGRIP Ice Core for the Last 16,000 Years – Glaciological and Paleoclimatic Implications, Earth and Planetary Science Letters, 405, 132–141, https://doi.org/10.1016/j.epsl.2014.08.022, 2014.

Gladstone, R. M., Payne, A. J., and Cornford, S. L.: Parameterising the Grounding Line in Flow-Line Ice Sheet Models, The Cryosphere, 4, 605–619, https://doi.org/10.5194/tc-4-605-2010, 2010.

Gulev, S., Thorne, P., Ahn, J., Dentener, F., Domingues, C., Gerland, S., Gong, D., Kaufman, D., Nnamchi, H., Quaas, J., Rivera, J., Sathyendranath, S., Smith, S., Trewin, B., von Schuckmann, K., and Vose, R.: Changing State of the Climate System, in: Climate Change 2021: The Physical Science Basis. Contribution of Working Group I to the Sixth Assessment Report of the Intergovernmental Panel on Climate Change, edited by Masson-Delmotte, V., Zhai, P., Pirani, A., Connors, S., Péan, C., Berger, S., Caud, N., Chen, Y., Goldfarb, L., Gomis,

M., Huang, M., Leitzell, K., Lonnoy, E., Matthews, J., Maycock, T., Waterfield, T., Yelekçi, O., Yu, R., and Zhou, B., pp. 287–422, Cambridge University Press, Cambridge, United Kingdom and New York, NY, USA, https://doi.org/10.1017/9781009157896.004, 2021.

Huybrechts, P.: Sea-Level Changes at the LGM from Ice-Dynamic Reconstructions of the Greenland and Antarctic Ice Sheets during the Glacial Cycles, Quaternary Science Reviews, 21, 203–231, https://doi.org/10.1016/S0277-3791(01)00082-8, 2002.

Imbrie, J. D. and McIntyre, A.: SPECMAP Time Scale Developed by Imbrie et al., 1984 Based on Normalized Planktonic Records (Normalized O-18 vs Time, Specmap.017), https://doi.org/10.1594/PANGAEA.441706, 2006.

Jakobsson, M., Mayer, L. A., Bringensparr, C., Castro, C. F., Mohammad, R., Johnson, P., Ketter, T., Accettella, D., Amblas, D., An, L., Arndt, J. E., Canals, M., Casamor, J. L., Chauché, N., Coakley, B., Danielson, S., Demarte, M., Dickson, M.-L., Dorschel, B., Dowdeswell, J. A., Dreutter, S., Fremand, A. C., Gallant, D., Hall, J. K., Hehemann, L., Hodnesdal, H., Hong, J., Ivaldi, R., Kane, E., Klaucke, I., Krawczyk, D. W., Kristoffersen, Y., Kuipers, B. R., Millan, R., Masetti, G., Morlighem, M., Noormets, R., Prescott, M. M., Rebesco, M., Rignot, E., Semiletov, I., Tate, A. J., Travaglini, P., Velicogna, I., Weatherall, P., Weinrebe, W., Willis, J. K., Wood, M., Zarayskaya, Y., Zhang, T., Zimmermann, M., and Zinglersen, K. B.: The International Bathymetric Chart of the Arctic Ocean Version 4.0, Scientific Data, 7, 176, https://doi.org/10.1038/s41597-020-0520-9, 2020.

Jansen, D., Franke, S., Bauer, C. C., Binder, T., Dahl-Jensen, D., Eichler, J., Eisen, O., Hu, Y., Kerch, J., Llorens, M.-G., Miller, H., Neckel, N., Paden, J., Riese, T., Sachau, T., Stoll, N., Weikusat, I., Wilhelms, F., Zhang, Y., and Bons, P. D.: Shear Margins in Upper Half of Northeast Greenland Ice Stream Were Established Two Millennia Ago, Nature Communications, 15, 1193, https://doi.org/10.1038/s41467-024-45021-8, 2024.

Johnsen, S. J., Clausen, H. B., Dansgaard, W., Gundestrup, N. S., Hansson, M., Jonsson, P., Steffensen, J. P., and Sveinbjørnsdottir, A. E.: A "Deep" Ice Core from East Greenland, Meddelelser om Grønland. Geoscience, 29, 22 pp.–22 pp., https://doi.org/10.7146/moggeosci.v29i.140329, 1992.

Johnsen, S. J., Dahl-Jensen, D., Dansgaard, W., and Gundestrup, N.: Greenland Palaeotemperatures Derived from GRIP Bore Hole Temperature and Ice Core Isotope Profiles, Tellus B: Chemical and Physical Meteorology, 47, 624–629, https://doi.org/10.3402/tellusb.v47i5.16077, 1995.

Lauritzen, M., Aðalgeirsdóttir, G., Rathmann, N., Grinsted, A., Noël, B., and Hvidberg, C. S.: The Influence of Inter-Annual Temperature Variability on the Greenland Ice Sheet Volume, Annals of Glaciology, pp. 1–8, https://doi.org/10.1017/aog.2023.53, 2023.

Lecavalier, B. S., Milne, G. A., Vinther, B. M., Fisher, D. A., Dyke, A. S., and Simpson, M. J.: Revised Estimates of Greenland Ice Sheet Thinning Histories Based on Ice-Core Records, Quaternary Science Reviews, 63, 73–82, https://doi.org/10.1016/j.quascirev.2012.11.030, 2013.

Lecavalier, B. S., Fisher, D. A., Milne, G. A., Vinther, B. M., Tarasov, L., Huybrechts, P., Lacelle, D., Main, B., Zheng, J., Bourgeois, J., and Dyke, A. S.: High Arctic Holocene Temperature Record from the Agassiz Ice Cap and Greenland Ice Sheet Evolution, Proceedings of the National Academy of Sciences, 114, 5952–5957, https://doi.org/10.1073/pnas.1616287114, 2017.

Leger, T. P. M., Clark, C. D., Huynh, C., Jones, S., Ely, J. C., Bradley, S. L., Diemont, C., and Hughes, A. L. C.: A Greenland-wide Empirical Reconstruction of Paleo Ice Sheet Retreat Informed by Ice Extent Markers: PaleoGrIS Version 1.0, Climate of the Past, 20, 701–755, https://doi.org/10.5194/cp-20-701-2024, 2024.

Lingle, C. S. and Clark, J. A.: A Numerical Model of Interactions between a Marine Ice Sheet and the Solid Earth: Application to a West Antarctic Ice Stream, Journal of Geophysical Research: Oceans, 90, 1100–1114, https://doi.org/10.1029/JC090iC01p01100, 1985.

Liu, Z., Otto-Bliesner, B. L., He, F., Brady, E. C., Tomas, R., Clark, P. U., Carlson, A. E., Lynch-Stieglitz, J., Curry, W., Brook, E., Erickson, D., Jacob, R., Kutzbach, J., and Cheng, J.: Transient Simulation of Last Deglaciation with a New Mechanism for Bølling-Allerød Warming, Science, 325, 310–314, https://doi.org/10.1126/science.1171041, publisher: American Association for the Advancement of Science, 2009.

MacGregor, J. A., Colgan, W. T., Fahnestock, M. A., Morlighem, M., Catania, G. A., Paden, J. D., and Gogineni, S. P.: Holocene Deceleration of the Greenland Ice Sheet, Science, 351, 590–593, https://doi.org/10.1126/science.aab1702, 2016.

Morlighem, M.: IceBridge BedMachine Greenland, Version 5, https://doi.org/10.5067/GMEVBWFLWA7X, 2022.

Morlighem, M., Bondzio, J., Seroussi, H., Rignot, E., Larour, E., Humbert, A., and Rebuffi, S.: Modeling of Store Gletscher's Calving Dynamics, West Greenland, in Response to Ocean Thermal Forcing, Geophysical Research Letters, 43, 2659–2666, https://doi.org/10.1002/2016GL067695, 2016.

Morlighem, M., Williams, C. N., Rignot, E., An, L., Arndt, J. E., Bamber, J. L., Catania, G., Chauché, N., Dowdeswell, J. A., Dorschel, B., Fenty, I., Hogan, K., Howat, I., Hubbard, A., Jakobsson, M., Jordan, T. M., Kjeldsen, K. K., Millan, R., Mayer, L., Mouginot, J., Noël, B. P. Y., O'Cofaigh, C., Palmer, S., Rysgaard, S., Seroussi, H., Siegert, M. J., Slabon, P., Straneo, F., van den Broeke, M. R., Weinrebe, W., Wood, M., and Zinglersen, K. B.: BedMachine v3: Complete Bed Topography and Ocean Bathymetry Mapping of Greenland From Multibeam Echo Sounding Combined With Mass Conservation, Geophysical Research Letters, 44, https://doi.org/10.1002/2017GL074954, 2017.

Mouginot, J. and Rignot, E.: Glacier Catchments/Basins for the Greenland Ice Sheet, https://doi.org/10.7280/D1WT11, 2019.

Nias, I. J., Nowicki, S., Felikson, D., and Loomis, B.: Modeling the Greenland Ice Sheet's Committed Contribution to Sea Level During the 21st Century, Journal of Geophysical Research: Earth Surface, 128, e2022JF006 914, https://doi.org/10.1029/2022JF006914, 2023.

Nielsen, L. T., Aðalgeirsdóttir, Gu., Gkinis, V., Nuterman, R., and Hvidberg, C. S.: The Effect of a Holocene Climatic Optimum on the Evolution of the Greenland Ice Sheet during the Last 10 Kyr, Journal of Glaciology, 64, 477–488, https://doi.org/10.1017/jog.2018.40, 2018.

Noël, B., Van De Berg, W. J., Van Meijgaard, E., Kuipers Munneke, P., Van De Wal, R. S. W., and Van Den Broeke, M. R.: Evaluation of the Updated Regional Climate Model RACMO2.3: Summer Snowfall Impact on the Greenland Ice Sheet, The Cryosphere, 9, 1831–1844, https://doi.org/10.5194/tc-9-1831-2015, 2015.

Noël, B., van de Berg, W. J., Lhermitte, S., Wouters, B., Schaffer, N., and van den Broeke, M. R.: Six Decades of Glacial Mass Loss in the Canadian Arctic Archipelago, Journal of Geophysical Research: Earth Surface, 123, 1430–1449, https://doi.org/10.1029/2017JF004304, 2018.

Noël, B., Van De Berg, W. J., Lhermitte, S., and Van Den Broeke, M. R.: Rapid Ablation Zone Expansion Amplifies North Greenland Mass Loss, Science Advances, 5, eaaw0123, https://doi.org/10.1126/sciadv.aaw0123, 2019.

Nowicki, S., Goelzer, H., Seroussi, H., Payne, A. J., Lipscomb, W. H., Abe-Ouchi, A., Agosta, C., Alexander, P., Asay-Davis, X. S., Barthel, A., Bracegirdle, T. J., Cullather, R., Felikson, D., Fettweis, X., Gregory, J. M., Hattermann, T., Jourdain, N. C., Kuipers Munneke, P., Larour, E., Little, C. M., Morlighem, M., Nias, I., Shepherd, A., Simon, E., Slater, D., Smith, R. S., Straneo, F., Trusel, L. D., Van Den Broeke, M. R., and Van De Wal, R.: Experimental Protocol for Sea Level Projections from ISMIP6 Stand-Alone Ice Sheet Models, The Cryosphere, 14, 2331–2368, https://doi.org/10.5194/tc-14-2331-2020, 2020.

Peltier, W. R.: GLOBAL GLACIAL ISOSTASY AND THE SURFACE OF THE ICE-AGE EARTH: The ICE-5G (VM2) Model and GRACE, Annual Review of Earth and Planetary Sciences, 32, 111–149, https://doi.org/10.1146/annurev.earth.32.082503.144359, publisher: Annual Reviews, 2004.

Rasmussen, S. O., Andersen, K. K., Svensson, A. M., Steffensen, J. P., Vinther, B. M., Clausen, H. B., Siggaard-Andersen, M.-L., Johnsen, S. J., Larsen, L. B., Dahl-Jensen, D., Bigler, M., Röthlisberger, R., Fischer, H., Goto-Azuma, K., Hansson, M. E., and Ruth, U.: A New Greenland Ice Core Chronology for the Last Glacial Termination, Journal of Geophysical Research: Atmospheres, 111, https://doi.org/10.1029/2005JD006079, 2006.

RGI Consortium: Randolph Glacier Inventory - A Dataset of Global Glacier Outlines, Version 7, https://doi.org/10.5067/F6JMOVY5NAVZ, 2023.

Schumacher, M., King, M. A., Rougier, J., Sha, Z., Khan, S. A., and Bamber, J. L.: A New Global GPS Data Set for Testing and Improving Modelled GIA Uplift Rates, Geophysical Journal International, 214, 2164–2176, https://doi.org/10.1093/gji/ggy235, 2018.

Shapiro, N.: Inferring Surface Heat Flux Distributions Guided by a Global Seismic Model: Particular Application to Antarctica, Earth and Planetary Science Letters, 223, 213–224, https://doi.org/10.1016/j.epsl.2004.04.011, 2004.

Solgaard, A., Kusk, A., Merryman Boncori, J. P., Dall, J., Mankoff, K. D., Ahlstrøm, A. P., Andersen, S. B., Citterio, M., Karlsson, N. B., Kjeldsen, K. K., Korsgaard, N. J., Larsen, S. H., and Fausto, R. S.: Greenland Ice Velocity Maps from the PROMICE Project, Earth System Science Data, 13, 3491–3512, https://doi.org/10.5194/essd-13-3491-2021, 2021.

Solgaard, A. M. and Kusk, A.: Greenland Ice Velocity from Sentinel-1 Edition 3, https://doi.org/10.22008/FK2/ZEGVXU, 2023.

Tabone, I., Robinson, A., Montoya, M., and Alvarez-Solas, J.: Holocene Thinning in Central Greenland Controlled by the Northeast Greenland Ice Stream, Nature Communications, 15, 6434, https://doi.org/10.1038/s41467-024-50772-5, 2024.

Tang, B.: Orthogonal Array-Based Latin Hypercubes, Journal of the American Statistical Association, 88, 1392–1397, https://doi.org/10.2307/2291282, 1993.

The IMBIE Team: Mass Balance of the Greenland Ice Sheet from 1992 to 2018, Nature, 579, 233–239, https://doi.org/10.1038/s41586-019-1855-2, 2020.

Vinther, B. M., Buchardt, S. L., Clausen, H. B., Dahl-Jensen, D., Johnsen, S. J., Fisher, D. A., Koerner, R. M., Raynaud, D., Lipenkov, V., Andersen, K. K., Blunier, T., Rasmussen, S. O., Steffensen, J. P., and Svensson, A. M.: Holocene Thinning of the Greenland Ice Sheet, Nature, 461, 385–388, https://doi.org/10.1038/nature08355, 2009.

Winkelmann, R., Martin, M. A., Haseloff, M., Albrecht, T., Bueler, E., Khroulev, C., and Levermann, A.: The Potsdam Parallel Ice Sheet Model (PISM-PIK) – Part 1: Model Description, The Cryosphere, 5, 715–726, https://doi.org/10.5194/tc-5-715-2011, 2011.